GEOPHYSICS®

First Application of the Marine Differential Electric Dipole for Offshore Groundwater Studies: A Case Study from Bat Yam, Israel

Journal:	*Geophysics*
Manuscript ID	GEO-2017-0162.R2
Manuscript Type:	Case Histories
Date Submitted by the Author:	26-Oct-2017
Complete List of Authors:	Haroon, Amir; Universitat zu Koln Mathematisch-Naturwissenschaftliche Fakultat, Geophysik und Meteorologie Lippert, Klaus; Universitat zu Koln Institut fur Geophysik und Meteorologie Mogilatov, Vladimir; IPGG SB RAS, Tezkan, Bulent; University of Cologne, Inst. of Geophysics & Meteorology
Keywords:	marine, time-domain, electromagnetics, groundwater, aquifer
Area of Expertise:	Electrical and Electromagnetic Methods
Note: The following files were submitted by the author for peer review, but cannot be converted to PDF. You must view these files (e.g. movies) online.	
Table1.tex	

First Application of the Marine Differential Electric Dipole for Groundwater Investigations: A Case Study from Bat Yam, Israel

Amir Haroon[1,2], **Klaus Lippert**[1], **Vladimir Mogilatov**[3] **and Bülent Tezkan**[1]

[1] *Institute of Geophysics and Meteorology, University of Cologne, Pohligstr. 3, 50969, Cologne, Germany*

[2] *Helmholtz Centre for Ocean Research, GEOMAR, Wischhofstr. 1-3, 24148, Kiel, Germany*

[3] *Novosibirsk State University, 630090 Novosibirsk, Russia*

(December 21, 2017)

GEO-2017-0162.R2

Running head: **Marine DED in Bat Yam, Israel**

ABSTRACT

The marine Differential Electric Dipole (DED) is applied for the first time to study a sub-seafloor groundwater body in the coastal region of Bat Yam, Israel. Previous marine long-offset transient electromagnetic (LOTEM) applications detected this freshwater body underneath the Mediterranean seafloor. The presented case study applies the novel DED method for the first time in the marine environment to further investigate this natural phenomenon. The main objectives are to locate the freshwater-seawater interface at the western aquifer edge and to identify the mechanism controlling this freshwater occurrence beneath the seafloor. The acquired step-on signals allow one to detect the freshwater body in the vicinity of the Israeli coastline at a depth of approximately 70 m beneath the seafloor. However, aquifer thickness is only poorly determined and may vary between 40 m and 100 m. A lateral resistivity contrast is observable between adjacent 1D inversion models and also

apparent in data profile curves that constrain the seaward extent of the detected resistive body to a distance of less than 4 km from the coastline. A subsequent 2.5D forward modeling study aims to find a sub-seafloor resistivity distribution that adequately explains all measured DED data simultaneously. The results further constrain the lateral extent of the resistive aquifer to approximately 3.6 - 3.7 km from the Israeli coast. Furthermore, the data indicates that the aquifer system may be susceptible to seawater intrusion as a superior data fit is achieved if a brackish water zone of approximately 3 Ωm with a lateral extent of less than 300 m is located at the head of the freshwater body.

INTRODUCTION

Groundwater reservoirs in coastal regions are particularly vulnerable to contamination due to the continuing natural threat of seawater rise and anthropogenic influences caused by increased urbanization. The consequence is often a deterioration of groundwater quality in terrestrial aquifer systems. In Israel, the issue of groundwater pollution is pronounced as population steadily increases and the coastal regions of the Mediterranean Sea are already densely populated. Moreover, the coastal aquifer is one of only three national groundwater reservoirs (Kafri and Goldman, 2006) and is heavily exploited. The salinity content of this aquifer has increased in the last decades mainly due to anthropogenic pollution and artificial recharge (Amir et al., 2013; Kafri and Goldman, 2006). The aquifer is replenished laterally by the Judean mountain aquifer and drains into the Mediterranean Sea. As illustrated in Fig. 1, the east-west extent of the aquifer from the Mediterranean Sea to the foothills is between 8 km in the North, and 30 km in the South with a thickness of 200 m or less (Amir et al., 2013). The units within the aquifer consist mainly of sand and calcareous sandstone which are separated by aquicludal clay formations near the coast that thin out towards the East. The aquifer is generally divided into four sub-aquifers named A, B, C, and D from top to bottom. The upper sub-aquifers A and B are phreatic and are prone to seawater encroachment throughout the entire Israeli coastal plain as saline water has been detected at these depth intervals (Kafri and Goldman, 2006). Kapuler and Bear (1970) assume that this also applies to the lower sub-aquifers. Kolton (1988) challenges their assumption, stating that the lower sub-aquifers (C and D) thin out underneath the Mediterranean Sea in the West and pass into a continuous shale sequence that blocks the lower sub-aquifers from seawater intrusion. Kafri and Goldman (2006) summarize observations that support both predictions of Kolton (1988) and of Kapuler and Bear (1970). For instance, the water age obtained from the lower sub-aquifers is older than that of the upper ones indicating a restricted fluid exchange between the upper and lower sub-aquifers. This suggests that the lower

Figure 1: *(a) Map of the coastal aquifer of Israel highlighted in dark-gray. The Palmahim area where the lower sub-aquifers are occupied by fresh water is illustrated in light-gray along with the measured DED profile (dashed black line). Image was modified after Amir et al. (2013). (b) Typical cross section of the Israeli coastal aquifer between P and P' indicated by the solid black line in (a). Near the coast, the aquifer is divided into four separate sub-aquifers named A through D that are divided by impermeable clay formations. Image modified after Kafri and Goldman (2006).*

aquifers are confined, whereas the upper ones are prone to seawater intrusion. On the other hand, the lower sub-aquifers are also intruded by saline water in other areas along the coastal plain of Israel suggesting that all sub-aquifers are susceptible to seawater intrusion.

To study the resistivity distribution of the subsurface, electromagnetic (EM) induction methods are commonly applied. These applications can distinguish a geological formation from its surroundings if a resistivity contrast exists. This is particularly useful when studying the salinity content of groundwater aquifers, as the pore-fluid salinity is directly proportional to the measured electrical resistivity (Archie, 1942). The measured resistivity will decrease for increasing pore fluid salinity. In Israel, Goldman et al. (1988) quantifies the resistivity of seawater saturated sediments at shallow depths beneath the surface between $0.5\ \Omega$m and $1.5\ \Omega$m, whereas freshwater saturated sediments will have resistivity values greater than $10\ \Omega$m (Kafri and Goldman, 2006). This resistivity contrast can be efficiently targeted using Controlled Source Electromagnetic (CSEM) methods.

The majority of marine CSEM applications are conducted in the frequency domain and focus on detecting resistive bodies embedded in conductive background environments. The most general application utilizes a horizontal electrical dipole (HED) transmitter exciting a continuous, low

frequency waveform along with multiple ocean-bottom EM receivers (OBEMs), e.g. Constable (2010). The application has proven effective, particularly for hydrocarbon studies, e.g. (Eidesmo et al., 2002; Ellingsrud et al., 2002). This lead to an increased attention to marine CSEM applications resulting in development of theory, e.g. Chave and Cox (1982) and more recently, development of 2D interpretation software, e.g. **?**Key (2016). However, in shallow sea environments with water depths below 100 m, the frequency-domain CSEM application as described above is rather ineffective. In part this is due to the masking effect of the airwave signal (Weidelt, 2007). Methods have been developed to mitigate the parasitic airwave signal and are summarized by Chen and Alumbaugh (2011). Yet, these approaches are often inaccurate due to simplified assumptions that might not hold for all settings. As demonstrated by Weiss (2007), an effective alternative approach in shallow sea environments is the time-domain CSEM application, discussed in e.g. Thomsen et al. (2007), Strack et al. (2008) and Tezkan et al. (2012).

Compared to the frequency-domain application described above, time-domain applications are often conducted using fixed-offset transmitter/receiver systems that are pulled along the seafloor and stop at each measuring location, e.g Schwalenberg and Engels (2011). In literature, the time-domain application is also often referred to as CSEM, or sometimes time-domain CSEM. We will stick to the convention of Long Offset Transient Electromagnetic (LOTEM) method (Strack, 1992). It should be mentioned that modifications of CSEM and LOTEM exist, where OBEMs are used in the time domain, e.g. Strack et al. (2008); Hölz et al. (2015) or fixed offset systems in the frequency domain, e.g. Bhuiyan et al. (2014); Sherman et al. (2017).

The motivation of the presented study dates back to an onshore in-loop transient EM (TEM) application conducted along the coastal plain of Israel to investigate the subsurface resistivity distribution (Kafri and Goldman, 2006). The authors detected regions of high and regions of low resistivity values within the depth range of the lower coastal sub-aquifers. Direct borehole salinity

measurements confirmed that regions of decreased resistivity are linked to aquifer systems containing saline water, whereas regions with increased resistivity values had aquifers occupied with fresh to brackish water (Kafri and Goldman, 2006). These regions were interpreted as locally blocked to the Mediterranean Sea, preventing seawater from intruding the aquiferous units. The largest region of interest is a 20 km long transect known as the Palmahim Disturbance, located between the cities of Ashdod in the South and Bat Yam in the North (cf. Fig. 1). Marine LOTEM measurements conducted in the framework of a joint project by the Geophysical Institute of Israel (GII), Israel Oceanographic and Limnological Research (IOLR), and the Institute of Geophysics & Meteorology, Cologne, Germany (IGM) between 2009 and 2011 confirmed the offshore extent of this freshwater body to approximately 3.5 - 4.2 km from the coastline (Goldman et al., 2011; Lippert et al., 2012; Lippert, 2015). However, the results did not enable an adequate answer as to why this region of the lower coastal sub-aquifer contains fresh groundwater, and whether the aquifer is blocked to seawater intrusion or not (Lippert, 2015). Especially the sparse data density around the assumed aquifer boundary prohibited an assessment of the freshwater-seawater interface.

In the extent of the joint project, Amir et al. (2013) conducted groundwater flow studies for the Palmahim area based on still unknown assumptions, i.e. the location of the freshwater-saltwater transition zone. The authors assumed an aquifer edge at 10 km from the coastline, which may be incorrect and could lead to false conclusions regarding the freshwater occurrence in the region. To further investigate the hydro-geological mechanism controlling the shape and location of the freshwater-seawater interface, a Differential Electric Dipole (DED) application was conducted in April 2016. Haroon et al. (2016) show that the excited EM field of a DED source is more sensitive to the lateral boundaries of resistive 3D structures compared to a HED source. Accordingly, the first attempted application of DED in the marine environment aims to use this increased sensitivity to locate the position of the freshwater-seawater interface and, additionally, derive information

regarding the structure of the mechanism controlling this freshwater occurrence.

The marine DED measurements were carried out with the research vessel Mediterranean Explorer from the non-profit organization EcoOcean.org. During four days of measurement, 22 receiver stations were acquired along the 5 km profile of Lippert (2015). Technical issues arose at five receiver stations which are not considered in the present study. Acquired data is first interpreted with 1D inversion using a self-developed forward algorithm that was implemented into an existing inversion routine. Subsequently, a 2.5D forward modeling study is conducted by calculating 2D subsurface resistivity models with the 3D finite difference algorithm of Druskin and Knizhnerman (1988, 1994). Thereby the 2D resistivity structures were extended into the third dimension allowing variations only with depth and profile direction. As data was only obtained along one transect, 3D resistivity variations are not considered. Although the forward operator is indeed 3D, we will refer to the study as 2.5D in the following to emphasize the considered 2D resistivity variations. In total, the modeling study included over 425,600 forward calculations.

Due to the bathymetry near the coastline of Bat Yam, resistivity variations are expected in two, maybe even three dimensions. However, Haroon (2016) demonstrates that a 1D inversion approach of step-on DED data leads to a realistic sub-seafloor resistivity structure, if certain conditions regarding the thickness of the overlying water column are respected. Yet, the 1D inversion approach is insufficient in analyzing the 2D/3D resistivity structure of the aquifer boundary. Accordingly, the 1D inversion models are used to constrain the model parameters in the subsequent 2.5D forward modeling study.

Unfortunately, a 2D inversion software for marine DED is presently not available. Therefore, a data fit is achieved by using a constrained forward modeling approach. For this, the model parameter space is divided into five parameters that are varied between minimum and maximum values

Figure 2: *(a) Sketch of a seafloor-based DED transmitter/receiver system consisting of a 400 m double-dipole antenna (yellow) and two inline electric field receivers of 50 m length (blue) that are connected to the transmitter antenna by segments of rope/chain at offsets of 370 m and 580 m, respectively. Note, receiver electrodes are located on the seafloor. The signal is guided to the KMS-820 acquisition unit located on the sea-surface. (b) Power spectrum and (c) excerpt of a measured inline voltage time series for an exemplary station from Bat Yam, Israel. A 50% duty cycle current step-function with a period of 2 s was applied.*

derived from the 1D inversion models. The forward response of all existing parameter combinations is calculated for all transmitter/receiver configurations. The main objectives are to delineate the freshwater-seawater interface, including its location along the profile and structure. The 2.5D forward calculations were carried out on the CHEOPS-Cluster at the University of Cologne between the beginning of June and end of August, 2016. An ensemble of resistivity models that best describe the measured DED data set is determined and evaluated. First, the models are analyzed according to the corresponding data fit at each receiver station in order to derive the location of the freshwater-seawater interface. Subsequently, an ensemble of best fit models is utilized to determine resistivity-depth combinations that best describe the measured DED data. Finally, a further block is introduced to the model at the aquifer head to investigate if data fits can be improved by simulating an intermediate brackish water zone. In this scenario, the aquifer is considered susceptible to seawater intrusion.

METHOD

The idea of applying a time-domain DED transmitter for shallow marine EM applications was theoretically presented by Haroon et al. (2016) using several 1D and 3D forward modeling studies. The DED transmitter can be seen as a simplification of a Circular Electrical Dipole (CED), which was first introduced by Mogilatov (1992) and practically realized by Mogilatov and Balashov (1996). Their CED transmitter consists of eight HEDs arranged in a concentric loop around a common central electrode (Mogilatov et al., 2016). The excited EM field of a surface-based CED transmitter is equivalent to that of a Vertical Electrical Dipole (VED). In shallow water, the conceived advantage of CED is that the antenna is not limited by the water column. However, substantial signal distortions caused by geometrical inaccuracies of the eight HEDs currently prohibit a marine CED application (Haroon et al., 2016). Therefore, the authors suggest to simplify the CED transmitter to a DED, which consists of only two HEDs arranged in line with a common central electrode (cf. Fig. 2a). The current in each dipole flows in opposite directions resulting in a double-lobe electric field excited above and below a seafloor-based transmitter (cf. Fig. 3). Appropriately, the central electrode has one polarity, whereas the two 'outer' electrodes have the other one. An exemplary power spectrum and the corresponding voltage time series are displayed in Fig. 2b and Fig. 2c, respectively. Electric field amplitude patterns of a step-on excitation in the *xz*-plane for a seafloor-based DED with 30 m water of 0.2 Ωm above and a homogeneous half-space of 1 Ωm below are illustrated in Fig. 3. Note, the black lines represent the horizontal layer boundaries. As time progresses after current injection, the electric field diffuses downward and outward from the transmitter. Similar to a HED source, the excited EM field of a DED is bimodal, consisting of both transverse electric (TE) and transverse magnetic (TM) mode in a stratified earth. Hence, for 1D resistivity distribution, the detectability of resistive layers is comparable to a HED transmitter (Haroon et al., 2016). However, as the excited field of DED is more focused underneath the transmitter, a higher

Figure 3: *Electric field amplitude in the xz-plane for a source-normalized seafloor-based DED transmitter at time delays of $t = 5.00e^{-5}$ s, $t = 7.01e^{-4}$ s, $t = 2.23e^{-3}$ s and $t = 2.65e^{-2}$ s after the current is switched on. The resistivity of the overlying 30 m water column is 0.2 Ωm and underlying half-space is 1 Ωm. The insulating air ($z < 0$ m) is defined at 10^8 Ωm. The black lines represent the horizontal layer boundaries of the sea surface ($z = 0$ m) and seafloor ($z = 30$ m).*

sensitivity to boundary effects of 2D/3D resistivity structures is the benefit (Haroon et al., 2016; Haroon, 2016).

Theoretically, Davydycheva and Rykhlinski (2011) discuss the application of a focused-source EM (FSEM) system that resembles the DED in a so-called axial configuration. The theoretical background and DC current patterns for FSEM are found in Davydycheva et al. (2006). Similar approaches referred to as Differentially Normalized EM (DNEM) are presented in Russian literature, e.g Bubnov et al. (1984); Legeydo et al. (1990, 1997); Mandelbaum et al. (2002). A patent for marine geo-electrical exploration with electrical current focusing was issued by Rykhlinskaya and Davydycheva (2014). The elementary difference to a DED system is that the differential electric field of DNEM or FSEM is obtained through the measured receiver signals. In contrast, the DED current pattern is directly of differential nature through the three-electrode transmitter and no further post-processing steps are required to obtain the increased focus underneath the transmitter/receiver. DNEM and FSEM experiments for hydrocarbon exploration are published by Veeken et al. (2009), Davydycheva and Rykhlinski (2009) and Davydycheva et al. (2015).

Measuring System

The developed DED measuring system is illustrated in Fig. 2a. The tow line is composed of the transmitter cable, and several segments of rope and chains with the receiver electrodes attached at the predefined positions. Chains were needed to keep the system stationary during the data acquisition phase. The current was guided from the Tx-platform at the surface to the central electrode and into each transmitter dipole on the seafloor with an additional cable. Receiver Ag/AgCl electrodes from SILVION Limited were connected at predefined positions along the tow line so that the midpoints of two 50 m inline receiver dipoles (referred to as E_r in the following images) were located at offsets of 370 m and 580 m, respectively. Due to the shallow water column, cables from each receiver electrode were guided to the sea surface and connected to a KMS-820 data acquisition unit from KMS Technologies. This concept was motivated by two main factors. First, project funds did not allow to redesign the acquisition units to fit into towable waterproof casing. Second, by keeping the receiver units on the surface, we could accurately synchronize transmitter and receiver via GPS time, which simplified the data processing. At each station, a current amplitude of approximately 25 A was injected through the transmitter antenna. Data were sampled at 10 kHz.

The vessel pulled the system to each desired position and would then relocate and anchor with stern facing the Tx platform. A connection was established via a 80 m jumper cable. Subsequently, current was injected for an average of 30 minutes. These long stacking times ensured good data quality due to the high noise level in the coastal vicinity and the limited signal strength of the applied DED system. This acquisition strategy proved successful, but is also time-consuming, impractical and should be reconsidered before future DED applications. The ship relocation is one aspect that can be avoided in the future by guiding the power through the tow line to a seafloor based transmitter unit. However, this could result in an additional noise source as the current will have to be led by

Figure 4: *Schematics of possible 2D resistivity models found in the coastal vicinity of Bat Yam, Israel. (a) The aquifer is assumed to be blocked from seawater encroachment. (b) Typical wedge-shape boundary characterizes the transition between freshwater aquifer and seawater saturated sediments. (c) Brackish-water zone is located at the head of the freshwater body, representing an open aquifer scenario. Transmitter stations were simulated every 100 m between 2500 m and 4500 m with an electric field receiver located at an offset of 580 m on either side of the transmitter. Note, a more detailed illustration of the Tx/Rx configuration is found in Fig. 5.*

one transmitter dipole prior to being split at the central electrode. Moreover, the question of precise synchronization between transmitter and receiver will be more challenging compared to the present case.

One challenge of applying a DED system is its susceptibility to signal distortions caused by geometric errors (Haroon et al., 2016). This issue becomes relevant if the dipole moment of one dipole exceeds that of the other. It is essential that the current amplitudes remain stable and that the antenna geometry is kept consistent throughout the measurement procedure. The task of equal current amplitudes in each dipole is technically challenging, but was solved by implementing additional current stabilizers, steel transmitter cables of equal length, and identically manufactured electrodes. Keeping a consistent geometry on the seafloor is far more challenging. Exact positioning is difficult to control and, as a result, signal distortions caused by geometrical inaccuracies may become relevant. This has been extensively studied and presented by Haroon et al. (2016) and Haroon (2016). The theoretical studies show that the effect of geometrical distortion can be reduced by elongating the transmitter antenna and interpreting step-on signals. For a 400 m DED antenna, an effective

length reduction of 2 m (one outer electrode is located 17.4 m off the line) or less will cause the resulting step-on transient to be shifted by a quasi time-independent factor of approximately 1% that may be accounted for in the inversion process by the use of a calibration factor (CF) (Haroon, 2016). This factor is commonly applied in LOTEM inversion to account for receiver misalignment, improper definition of gain, offsets, current, etc. (Strack, 1992). During the measurement, positioning buoys indicated the system alignment at the sea surface. Throughout the measurement these were fairly consistent and the acquired step-on signals did not exhibit clear distortions that would suggest a severe misalignment of the transmitter or receiver. This is underlined by the profile plots (cf. Fig. 7) that would appear more erratic in case of geometrical distortions.

PRELIMINARY MODELING STUDIES

Prior to conducting the marine DED survey off the coast of Bat Yam, several 2.5D modeling studies were conducted using the 3D forward algorithm of Druskin and Knizhnerman (1994) to investigate the edge effects of the assumed 2D resistivity structure on the DED electric field response. The modeling studies show that profile plots are effective in locating the transition zone between the freshwater aquifer and the seawater saturated sediments. To investigate different hydro-geological scenarios at this western aquifer boundary, three 2D resistivity models are utilized, all based on the previous marine LOTEM results of Lippert (2015). Sketches of these models are shown in Fig. 4.

The models shown in Fig. 4 are identical in terms of resistivity and depth values. Solely the shape of the western aquifer boundary is altered. The first model represents a blocked aquifer scenario that is characterized by a sharp, vertical interface (cf. Fig. 4a). In this case, the lower sub-aquifer passes into an aquicludal shale sequence that prohibits seawater from interacting with the freshwater (Kolton, 1988; Kafri and Goldman, 2006). The terrestrial observations of Kafri

and Goldman (2006) and the marine LOTEM experiments of Lippert (2015) indicate that this scenario is likely due to the freshwater occurrence within the lower coastal sub-aquifers. The second model, illustrated in Fig. 4b, is characterized by a sharp, wedge-form that may represent a typical freshwater-seawater interface as found in many coastal aquifer systems around the world. The third model (shown in Fig. 4c), assumes an interaction between the saline and fresh water. Consequently, a zone of decreased resistivity (compared to the fresh water) is located at the head of the aquifer system. This zone represents a gradual transition of brackish water between the resistive freshwater aquifer and the conductive seawater saturated sediments. In this case, the coastal aquifer is assumed to be open, and as a result, susceptible to seawater intrusion. Note, for all scenarios, the edge to the seawater-saturated sediments is assumed to be located at 3500 m from the coastline, which is located at $x = 0$ m. The aquifer has a constant depth of 100 m beneath the sea surface within the area of investigation and does not vary laterally. The bathymetry model is derived from a nautical map and is similar to the true bathymetry found in Bat Yam.

The calculated profile runs perpendicular to the 2D resistivity structure of the freshwater-seawater interface. The synthetic DED data is calculated for a seafloor-based, 400 m DED transmitter antenna at 1 A current. At an offset of 580 m, the inline electric field is calculated on either side of the transmitter (cf. Fig. 5). The TX-dipole length and offset corresponds to the system applied in Israel. As illustrated in Fig. 5, the receiver is either located on the land-side of the transmitter (referred to as Rx-Land) or on the sea-side of the transmitter (referred to as Rx-Sea). In the following, signals of either configuration are examined.

Selected delay times are chosen for the profile plots from the maximum normalized response acquired using 1D modeling studies (Haroon et al., 2016). In Fig. 5, the signal amplitudes are plotted as a function of the receiver position along the profile. Accordingly, for a specific transmitter location, the curves of Rx-Land are shifted towards the coast, whereas the curves of Rx-Sea are

Figure 5: *Profile plots at selected time-delays of* 4.6 *ms (squares) and* 10 *ms (triangles) after current is switched on. The Blockage, Intrusion, and Brackish-Water models of Fig. 4a, b, and c are displayed by red, blue, and black colors, respectively. In the left image the receiver is located between transmitter and shoreline (Rx-Land). In the right image the receiver is located towards the sea-side of the transmitter (Rx-Sea). The gray background color indicates the lateral extent of the freshwater aquifer.*

shifted towards the sea. Assumed direction of tow is also displayed for reference, but does not suggest an actual towing phase. The lateral extent of the aquifer from the coastline is highlighted by the gray shaded background. Each figure contains six curves corresponding to the Blockage, Intrusion, and Brackish-water aquifer models of Fig. 4. These are displayed by red, blue, and black colors, respectively. The two selected time-delays of 4.6 ms and 10 ms are illustrated by square and triangular markers.

If Rx-Sea is considered (cf. Fig. 5-right), the information regarding the lateral resistivity discontinuity of the sub-seafloor aquifer system is registered as the receiver passes over the edge. Signal amplitudes increase as the receiver approaches the interface and reach a maximum above the edge. This behavior is different for Rx-Land (cf. Fig. 5-left), where the response of the aquifer edge is registered as the transmitter passes over the structure. Although, either tow direction is sufficient to locate the discontinuity in resistivity, it appears more apparent for Rx-Land. Amplitude variations of the individual curves seem more prominent for this configuration.

Based on the calculated profile curves, different hydro-geological scenarios at the western boundary are observable. A brackish water zone at the head of the aquifer is distinguishable from

the other two scenarios by the gradual slope of the profile curves due to the lower resistivity contrast between the background sediments and the brackish water. No obvious difference is noticeable between the curves of the Blockage (red) and Intrusion (blue) model. Hence, a clear distinction between a vertical and wedge-shaped boundary is not observable. Solely the interaction between the fresh and saline water in form of a brackish water zone is distinguishable from the other two models provided a sufficient station density is achieved.

The 2.5D forward modeling studies show that DED is effective in locating the lateral extent of the sub-seafloor aquifer using profile curves that exhibit an increase or decrease of signal amplitude if transmitter or receiver cross the 2D resistivity structure. Yet, the transmitter-receiver configuration and tow-directions need to be considered in this assessment due to the asymmetric behavior of the signals. Otherwise, the position of the aquifer boundary may be misinterpreted by a distance equaling the corresponding offset. The main conclusion of the presented forward modeling study is that DED step-on signals of this particular configuration can differentiate between the Brackish-Water model and the other two boundary scenarios, but cannot distinguish between a vertical or wedge-shaped boundary at the freshwater-seawater interface.

GEOPHYSICAL SURVEY

In April 2016, a marine DED survey was carried out on the profile of Lippert (2015) near the Mediterranean coastline of Bat Yam, Israel. The four-day survey was conducted with the research vessel “Mediterranean Explorer” from EcoOcean. In total, 17 receiver stations were measured along a 4 km transect. The survey design is based on the marine LOTEM experiment of Lippert (2015) that indicates the presence of a resistive body extending from the coastline to approximately 3.5 km - 4.2 km off the Israeli shore. This resistive layer was found to be a lower sub-aquifer belonging

Figure 6: *Map of the measurement area and survey geometry including positions of the measured inline receiver dipoles marked by black triangles and labeled p01FR through p17NR (from East to West). Transmitter centers are marked by red squares. The profile is interrupted due to a gas pipeline and a corresponding No-Anchor-Zone, which is bounded by the $\perp$ in the nautical map. Background map provided by the IOLR in Haifa. The left map of the coastal aquifer of Israel is modified after Amir et al. (2013)*

to the Mediterranean coastal aquifer system of Israel (Kafri and Goldman, 2006; Goldman et al., 2011; Lippert, 2015). However, due to the sparse data density of the marine LOTEM experiment, the transition between the resistive aquifer and the conductive marine sediments can only be assumed between two electrical field receivers located more than 400 m apart.

The primary aim of the presented study is to investigate the seaward extent of the resistive freshwater aquifer including the hydro-geological mechanism controlling the freshwater-seawater interface. The profile runs perpendicular to the coastline directly crossing the assumed transition zone. The acquired receiver stations are displayed in Fig. 6 by black triangles labeled p01FR through p17NR. The number describes the location along the profile: 01 being closest to the shoreline. The additional tags NR or FR refer to the receiver utilized at the corresponding station. Stations tagged NR were measured by the near (370 m offset), whereas stations tagged FR were measured by the far (580 m offset) receiver, respectively. The profile is interrupted between p06FR and p07FR due to the No-Anchor-Zone bounded in Fig. 6 by $\perp$. At the center of this zone, a gas pipeline runs from Northwest to Southeast. The system was deployed so that the receivers are located closest to the No-Anchor-Zone. Therefore, different tow directions exist on either side. In Fig. 6, the transmitter

stations are marked by red squares and labeled according to the measurement day in chronological order, e.g. Tx2-1: Day two, station one. Due to fishing in the area, the complete system was deployed and recovered each survey day.

Data Example

Measured time-domain EM data is generally superimposed by periodic and sporadic noise contributions. A single recorded current step-function generally suffers from poor SNR. The main periodic noise is often the 50 Hz frequency (and uneven harmonics) from the local power network. In most cases, sporadic noise also appears in the measured time series in the form of voltage spikes, drifts, steps, or white noise. These are a prominent feature in shallow marine EM experiments where motion induced noise caused by waves and currents are present. In any case, the superimposing noise needs to be removed from the time series prior to the interpretation. The data processing is a crucial step as an improper processing scheme will falsify or even prohibit an interpretation. In the applied approach, the data is processed by digital filtering techniques to eliminate periodic noise, followed by cluster analysis and log-gating/gate-stacking scheme (Munkholm and Auken, 1996; Hölz et al., 2015) to improve SNR.

The data error is approximated as absolute difference between voltage of the third and first quantile of the sorted amplitudes, divided by 1.35. This is the standard error approximation for LOTEM data processing and is well-suited for selective stacking schemes (Scholl, 2005). Before stacking, the measured data in each time gate is sorted and a certain percentage of the largest and smallest values are excluded. The percentage value is determined by a preceding quantile-quantile analysis. This processing scheme is robust against sporadic noise sources. Additionally, a minimum relative error floor of 1% is assigned.

Figure 7: *Profile plots at several time-delays derived from processed transients measured by the far receiver (FR) at an offset of* 580 *m. Data errors are indicated by the plotted error bars and are derived from the distribution of the measured signals in the robust stacking scheme (see text for further details).*

The six stations on the land-side of the No-Anchor-Zone (p01 - p06) are expected to be above the freshwater aquifer. The remaining stations, located on the sea-side of the No-Anchor-Zone (p07 - p17) are assumed to be either above the aquifer, the saltwater-freshwater transition zone, or a half-space consisting of seafloor sediments. To identify lateral resistivity discontinuities, profile plots are a useful preliminary interpretation tool (cf. Fig. 5). Several delay-times of the step-on data measured at an offset of 580 m are displayed as a function of their receiver position along the profile in Fig. 7.

The data qualitatively resembles the synthetic data presented in Fig. 5 for similar delay times. This applies to both curve shape and amplitude. Hence, a comparable lateral resistivity contrast as derived from LOTEM data is assumable. Between 3000 m and 4000 m from the coastline, electric field amplitudes clearly decrease, indicating a decrease in resistivity within the subsurface seawards. Similarly to the observations made using synthetic data in Fig. 5, the transition can be predicted between 3600 m and 3800 m. However, the data gap of the No-Anchor-Zone prohibits a more precise distinction, as the maximum field amplitude is not mapped by the data and can only be assumed. An additional 2D interpretation using forward modeling is necessary to further constrain the lateral extent of the resistive aquifer.

1D INVERSION

A 1D inversion approach is applied to derive a subsurface resistivity model for each transmitter-receiver configuration. In the following, two separate inversion algorithms generally referred to as Occam and Marquardt are applied to minimize ambiguity of the interpretation. The Occam inversion scheme for EM applications was introduced by Constable et al. (1987) and applied to LOTEM data by Hördt et al. (1992b). In the following, 1D Occam inversion models using the first roughness constraint are displayed. For the stations measured on the land-side of the No-Anchor-Zone, the 1D Occam inversion models indicate that the sub-seafloor resistivity structure is best described by an intermediate resistive body, embedded between two conductive layers above and below. Accordingly, a three-layer Marquardt inversion following Jupp and Vozoff (1975) was conducted for all stations along the profile, including model parameter resolution studies using Singular Value Decomposition (SVD) analysis of the weighted Jacobian (Edwards, 1997). Note, the Occam inversion routine attempts to find the smoothest model for the desired target misfit of $\chi = 1$, whereas the Marquardt inversion truncates if the target misfit of $\chi = 1$ is surpassed. Consequently, the Occam inversion models are generally fitted with $\chi \approx 1$ and Marquardt models with $\chi < 1$.

For each station, the water depth at the transmitter is acquired from multi-beam data and fixed for the process of inversion. The water resistivity was derived from in-situ measurements presented by Lippert (2015) and remains constant at a value of $0.2\ \Omega$m. In the following, 1D inversion results are displayed as a cross-section to convey a quasi-2D impression of the subsurface resistivity structure. Note, adjacent models have no mathematical connection within the inversion process. First, the Occam models using the first roughness constraint (R1) are calculated following Constable et al. (1987). The R1 regularization constrains the resistivity gradient, enforcing a smooth variation with depth. Sudden resistivity jumps are penalized. The final Occam models are then used to derive

Figure 8: *(a) 1D Occam and (b) Marquardt inversion models. The colored bars are located at the position of each corresponding receiver along the profile and describe the sub-seafloor resistivity structure. Light colors represent resistive, dark colors conductive structures. The data misfit is labeled above each graph. Stations are indicated by the red numbers at the bottom of each bar-graph.*

a starting model for the Marquardt inversion. Occam inversion models are displayed in Fig. 8a, and Marquardt in Fig. 8b. The shoreline is located at 0 m of the profile (extended towards the Southeast). The stations are labeled from right to left, station 01 through 17 and correspond to the station numbers in Fig. 6.

The data fit between measured and calculated data is expressed as χ value, which is defined as

$$\chi = \sqrt{\frac{1}{N}\sum_{i=1}^{N}\frac{(y_i - f_i(\mathbf{p}))^2}{\triangle y_i^2}}. \tag{1}$$

N describes the number of data points, y_i the measured electric field at time-index i, $f_i(\mathbf{p})$ the calculated datum at i for the model vector $\mathbf{p}$ of size M, and $\triangle y_i$ the corresponding data error estimation at index i. The data misfit is labeled above each inversion model in Fig. 8. Note, a $\chi \approx 1$ indicates an ideal data fit within the error bounds. If a misfit of $\chi < 1$ or $\chi > 1$ is reached, the data is perceived to be over- or under-fitted, respectively.

The Occam inversion models of stations 01 through 06 show a resistive layer of approximately 30 Ωm in the depth range of 70 m to 150 m located between coastline and No-Anchor-Zone. Above and below, more conductive regions of 0.7 Ωm to 1.5 Ωm are observable. These values correspond

to Goldman et al. (1988) and are interpreted as sediments saturated with saline water. The resistivity values of the intermediate layer are in the expected range of freshwater saturated coastal sediments in Israel (Kafri and Goldman, 2006). Aside from station 02, all stations located to the East of the No-Anchor-Zone coincide in terms of resistivity-depth structure. Only Station 02 differs from the remaining stations located east of the No-Anchor-Zone, as no resistive intermediate layer is apparent in the inversion model. Since all other stations located to east of the No-Anchor-Zone show a consistent image with an intermediate resistive layer, Station 02 is assumed erroneous and will be revisited in the description of Marquardt inversion models.

East of the No-Anchor-Zone, a lateral resistivity variation is noticeable. The receivers located closest to the No-Anchor-Zone (stations 07 through 10) show a resistivity increase in the depth range of the assumed freshwater aquifer. However, the values fail to reach the ones on the land-side. This may suggest, that the freshwater-seawater transition zone is occupied by brackish water implying an aquifer susceptible to seawater encroachment as suggest by Kapuler and Bear (1970). Yet, due to the expected 2D/3D subsurface resistivity structure in this region, a 1D interpretation may be insufficient meaning that the resistivity-depth structure of the 1D inversion models may be inconsistent due to the effect of the aquifer boundary. At minimum a 2D interpretation is needed to adequately describe the data measured in this region. For the remaining stations 11 through 17, the sub-seafloor resistivity structure is rather homogeneous. A resistive intermediate layer is not necessary to obtain an adequate data misfit of $\chi \approx 1$.

A three-layer starting model was derived from the Occam inversion models for the Marquardt inversion. The Marquardt inversion algorithm is parametrized to solve for layer resistivity and thickness of the layered-earth model. Note, although three-layers are not necessary to fit the data for stations 11 through 17, the starting model was kept consistent for a better comparison of the SVD analysis. The Marquardt inversion models of stations 01 through 06 show a consistent image of the

sub-seafloor resistivity structure with an intermediate resistive layer embedded between conductive layers. For station 02, a resistive layer is now also apparent, but is attributed the chosen starting model and is generally not necessary to fit the data. Again, stations 07 through 10 also indicate a resistive intermediate structure of decreased resistivity values, whereas stations 11 through 17 are rather homogeneous or indicate a conductive second layer. However, further analysis shown in Fig. 9 shows that the intermediate layer at these stations is poorly resolved and irrelevant to fit the data.

The data along with the corresponding residual errors defined as $(y_i - f_i(\mathbf{p}))/\triangle y_i$ at the selected stations p01FR, p08FR and p15FR are displayed in Fig. 9a, b, and c for the Occam R1 (solid line) and Marquardt (dashed line) inversion models, respectively. These stations are chosen exemplarily as they are located above the aquifer, freshwater-seawater transition zone, and conductive half-space. The displayed transients have $\chi \leq 1$, implying a data fit within the error bounds. No systematic tendency of data misfit is observable in the residual errors as calculated transients are within the error estimates. However, one apparent feature is the superior data fits of the Marquardt inversion models. This is related to the truncation procedure as described earlier and does not reflect the superiority of a Marquardt inversion models.

In order to analyze the resolution of resistivity and thickness values, we follow the statistical eigenparameter analysis presented by Strack (1992) and Edwards (1997). A perturbation of one model parameter may cause a significant alteration of the data curve that may not be unique; and varying the value of other parameters (or a combination of parameters) may produce a similar displacement. Consequently, it cannot be argued that the model parameter is resolved by the data (Swidinsky et al., 2012). This problem of model parameter inter-correlation is addressed in the eigenparameter statistical analysis (Edwards, 1997). The approach allows a clear assessment of a multi-parameter model from an experiment with associated standard errors (Swidinsky et al., 2012).

Figure 9: *(a-c) Data misfit and (d-f)* ***V****-matrix coefficients for station p01FR (left), p08FR (center) and p15FR (right). The measured data in the top panel is displayed by black markers including the corresponding error estimates that are illustrated as error bars. The synthetic response is displayed by solid and dashed black lines for Occam and Marquardt models, respectively. Beneath each image in the top-panel, residual errors are plotted for better reference of the data fit. The shaded zone indicates where the measured data is fit within the error bounds at each datum. The bottom panel displays the coefficients of the* ***V****-matrix. Black circles represent positive, white circle negative values. The radius of each circle is proportional to the coefficient weight. For further details refer to text.*

The weighted Jacobian or sensitivity matrix $\mathbf{J}$ contains the information on how the data are changed by small changes of the model. The content of $\mathbf{J}$ can be analyzed using a SVD where

$$\mathbf{J} = \mathbf{USV}^T. \tag{2}$$

$\mathbf{J}$ is a $N \times M$ matrix, which is decomposed into the unitary $N \times P$ matrix $\mathbf{U}$, the diagonal $P \times P$ matrix $\mathbf{S}$, and the unitary $M \times P$ matrix $\mathbf{V}$. In this case $\text{rank}(\mathbf{J}) = P \leq \min(M, N)$ as P number of non-zero singular values exist. The columns of $\mathbf{V}$ are called the eigenparameters (EPs) that are used to analyze the combination of original model parameters which are effectively resolved by the data (Scholl and Edwards, 2007).

Figure 9d through Fig. 9f show the SVD analysis for the selected stations p01FR, p08FR and p15FR following the visual approach presented by Strack (1992). Displayed are the entries of

matrix $\mathbf{V}$ using circles of certain radii and shading along with the corresponding standard error of the eigenvalues $\triangle(EV_{par})_i = 1/S_{ii}$ obtained from the diagonal matrix $\mathbf{S}$. The EPs are sorted according to the magnitude of their corresponding eigenvalue. The circle radii are proportional to the weight; positive weights are black, negative weights white. In each row, a coarse upper bound on the standard error $\triangle_{max}$ is given, which is defined as (Hölz et al., 2015)

$$\triangle_{max}(p_j) = \sum_{k=1}^{M} \left| \frac{V_{jk}}{S_{kk}} \right|, \tag{3}$$

where p_j is a specific value of model parameter vector $\mathbf{p}$. The error in a specific model parameter is only valid if it is small compared to unity as only linear changes are considered (Edwards, 1997). If the standard error is predicted larger than unity, a non-linear technique has to be adopted to find an error bound. In this case, no assessment regarding the model parameter resolution is feasible in the scope of this approach.

The SVD analysis of station p01FR presented in Fig. 9d exhibits more than one dominant entry for each EP. For example, EP1 (displayed in the first column of Fig. 9d) can be interpreted as the linear combination

$$EP1 \approx V_{11} \cdot log_{10}(\rho_1) + V_{41} \cdot log_{10}(d_1). \tag{4}$$

In terms of physical parameters, EP1 at station p01FR is considered as the ratio ρ_1/d_1 due to the negative sign of the coefficient V_{41}. Following this concept, the second column of Fig. 9d is the reciprocal resistivity-thickness product of the same parameters, with additional influences of ρ_2. Thus, ρ_1 and d_1 can be resolved individually by EP1 and EP2 as the corresponding errors $\triangle_{max}$ are also much smaller than unity. EP3 through EP5 share various combinations of the remaining model parameters ρ_2, ρ_3, and d_2. With ρ_3 being least relevant as its main contribution exists in EP5.

Figure 10: *Sketch of the 2D resistivity model utilized in the 2.5D forward modeling study. The model parameters ρ_1, ρ_2, d_1, d_2, and x_a are varied while seawater and land resistivity remain constant at 0.2 Ωm and 10 Ωm, respectively. At the air interface, integral boundary conditions are applied. The black triangles indicated the receiver locations along the profile. Selected station numbers are displayed beneath for reference.*

At Station p08FR located above the predicted freshwater-saltwater transition zone displayed in Fig. 9e, the circle distribution differs from station p01FR. EP1 and EP2 are sensitive to the original model parameters ρ_1 and d_1. However, the only relevant contribution of EP3 comes from ρ_3, indicating a well-resolved lower half-space. In contrast, ρ_2 and d_2 are only moderately to poorly resolved at p08FR. Due to the expected 2D/3D resistivity structure of the aquifer edge in this region, it is debatable if the 1D resolution studies are significant.

In Fig. 9f, the SVD at p15FR is displayed. EP1 has one dominant entry associated to the model parameter ρ_1 (seafloor sediments). The values of $\triangle_{max}$ indicate that ρ_2 and d_2 are not resolved with the linear approach as the values exceed unity. $\rho 3$ is well-resolved in EP4, but has a similar value to ρ_1. This confirms the inversion models of Occam, which indicate a homogeneous sub-seafloor resistivity structure.

The 1D interpretation of the measured marine DED data indicates the presence of a resistive layer located between the coastline and the No-Anchor-Zone. It is apparent in the 1D inversion models of stations p01FR through p10FR, and possibly extends to around 3500 m from the coast. This structure is interpreted as the freshwater aquifer. It disappears in the continuation of the profile and is not detectable at stations p11FR through p17NR. This indicates a lateral resistivity variation

Table 1: *Model parameters tested in the 2.5D forward modeling study to fit the measured DED data. For the stations of Zone B (cf. Fig. 6), all combinations are tested. Stations of Zone A are only tested for the resistivity and thickness parameters and not for variations of x_a.*

along the profile, which is supported by the shape of the measured profile curves (cf. Fig. 7). These exhibit a clear decrease of the inline electric field amplitude in the continuation of the profile towards the sea. However, due to the expected 2D/3D resistivity structure of the subsurface and the data gap of the No-Anchor-Zone, a clear distinction of the aquifer edge is difficult to derive from the measured data and 1D inversion models alone.

The 1D inversion models are utilized to derive a simplified 2D sub-seafloor resistivity model consisting of the five variable model parameters shown in Fig. 10. Specifically, these are the sediment resistivity ρ_1, the aquifer resistivity ρ_2, the depth of the aquifer from the sea surface d_1, the aquifer thickness d_2, and the lateral position of the aquifer boundary from the coast x_a. For the following forward modeling studies, these parameters are varied between minimum and maximum values as stated in Tab. 1. The shape of the aquifer boundary is assumed to be vertical. Additionally, the resistivity values for land and the sea are defined constant at $10\ \Omega$m and $0.2\ \Omega$m, respectively. The bathymetry model is derived from multi-beam data provided by the IOLR and remains constant throughout the modeling study. Also, no lateral depth variation of the aquifer is considered.

2D INTERPRETATION

The standard interpretation of marine LOTEM applications and, in particular, DED still lacks a 2D inversion. In the following, 2D resistivity models are calculated using the 3D finite difference forward algorithm of Druskin and Knizhnerman (1988); Hördt et al. (1992a); Druskin and Knizhnerman (1994) and follows two main objectives. The first objective is to locate the western aquifer boundary along the profile using the DED data obtained in Zone B, west of the No-Anchor-Zone (cf. Fig. 6). The second objective is to derive a 2D resistivity model that identifies if the sub-seafloor aquifer is prone to seawater intrusion. For the first objective, the subsurface is subdivided into the five variable model parameters listed in Tab. 1 and combinations of all parameters are tested. This approach results in a large number of possible combinations making the 2.5D forward modeling study computationally expensive. In total, over 425,600 forward calculations were conducted in order to identify an ensemble of best fit models that adequately explain the measured data. For the second objective, an additional block is introduced to investigate if the data fit is further reduced. An improvement could indicate the possibility of an open aquifer scenario where seawater intrusion is occurring.

The 2.5D forward modeling study adheres to the following procedure to process and analyze the calculated transients and compare them to the measured data.

1. Calculate synthetic data for all parameter combinations listed in Tab. 1 and all transmitter-receiver configurations.

2. A comparison between the calculated transients and the measured data is only feasible if the system response, including shape of the current step-function is taken into account (Strack, 1992). Accordingly, a convolution is conducted for each calculated transient and the measured system response. Subsequently, the convolved data is interpolated to the time samples of the

processed data.

3. A χ is calculated according to Eq. 1. The minimum relative data error at each datum is increased to account for numerical *sldmem3t* uncertainty. Magnitude of the additional error is derived by comparing the *sldmem3t* response to a synthetic forward solution for a 1D resistivity model. Furthermore, a line search for a CF between 0.9 and 1.1 is conducted to achieve the optimal data fit for each model. The CF accounts for small calibration effects in the electric field including transmitter/receiver inaccuracies, coupling, etc. As the CF for each model is confined to a small range, the applied CF is not considered in the evaluation of the best fit models.

4. The measured receiver stations are subdivided into two domains called Zone A and Zone B. Zone A is located east of the No-Anchor-Zone and includes stations p01FR through p06FR. All remaining receivers are located in Zone B. We will confine the investigation of quantifying the aquifer boundary location to receivers of Zone B. Zone A stations are only utilized to determine the remaining four model parameters. This confinement is supported by 1D resistivity models, which indicate that the aquifer edge is expected west of the No-Anchor-Zone. By applying this approach, we avoid 215,040 additional forward calculations without compromising the conclusiveness of the 2.5D forward modeling study. After locating the aquifer boundary, an ensemble of 2D resistivity models is derived that all lie within a 20% threshold of the best fit model. These models are utilized to discuss the subsurface resistivity structure.

5. Finally, we investigate if the aquifer is susceptible to seawater intrusion by introducing a further block into the best fit 2D resistivity model at the aquifer head. This block represents the open-aquifer scenario where a gradual transition between salt- and freshwater is apparent in the model (Amir et al., 2013). The focus will lie on analyzing whether the data fit can

Figure 11: *Bar graphs displaying the accumulation of models reaching $\chi \leq 1$ to identify the most likely position of the western aquifer boundary. The left figure shows stations p07FR through p11FR. The right image contains p12NR through p17NR. Each receiver is represented by a different color. In total, 58,240 forward models were tested at each receiver site.*

be further improved by the introduced block. Lateral extent and resistivity of the block are varied while keeping the remaining model parameters fixed.

As mentioned above, synthetic data at each Zone B receiver is calculated for all possible model parameter combinations listed in Tab. 1. Thereby, 4480 different combinations are tested for each of the 13 x_a values between 2800 m and 4000 m. Hence, combinations of the remaining resistivity and depth parameters are repetitive for each value of x_a. Accordingly, the most likely value of x_a is where the accumulation of resistivity models achieving a $\chi \leq 1$ is greatest. Cumulative bar graphs for each value of x_a are shown in Fig. 11. The stations are divided into two images for better representation. Based on the profile curves in Fig. 7, stations p07FR through p11FR are expected above the aquifer boundary as these exhibit the steepest descent in electric field amplitude. Stations p12NR through p17NR are located further west and are expected to be less influenced by the effects of the lateral resistivity contrast.

The results in Fig. 11 indicate that the aquifer boundary is likely located between 3600 m and 3700 m, slightly favoring the former. A distinct increase of 2D resistivity models achieving a $\chi \leq 1$ is apparent between station p07FR through p11FR for these two values of x_a. Receivers p07FR through p09FR favor a boundary at 3600 m, whereas receivers p10FR and p11FR support an aquifer

Figure 12: *Scatter plots displaying model parameter distribution for the ensemble of best fit models: (a) ρ_1, (b) ρ_2, (c) d_1 and (d) d_2 vs. the data fit χ. The x-axis of each sub-figure displays the entire investigated model parameter space. The black and red markers represent the model parameter distribution for models with $x_a = 3600$ m and $x_a = 3700$ m, respectively. The blue markers show the model parameter distribution obtained for receivers located in Zone A.*

edge at 3700 m from the coastline. At receivers p12NR through p17NR (Fig. 11-right), models with $\chi \leq 1$ are found for all x_a values. This indicates that the measured signals are not influenced by x_a and ideal data fit is reached for certain combinations of the four remaining model parameters. Specifically, this applies to receivers p14FR through p17NR.

Best fit 2D resistivity models are derived for values of $x_a = 3600$ m, $x_a = 3700$ m in Zone B, and independent of x_a in Zone A. Note, the models of Zone A and Zone B are treated individually. Differences and similarities in the model parameter distribution are discussed and illustrated in Fig. 12. All resistivity models that achieve a data fit within 20% of the best fit model for each group are considered equivalent. The distribution of ρ_1, ρ_2, d_1, and d_2 for all equivalent models are displayed by scatter plots in Fig. 12. The black markers represent the models with $x_a = 3600$ m, the red markers models with $x_a = 3700$ m, and the blue markers the values obtained by the receivers located in Zone A. Generally, the model parameter distribution of the considered best fit models are fairly consistent. The exception is ρ_1, which lies between 1.3 Ωm and 1.7 Ωm in Zone B, but does not exceed 1 Ωm in Zone A. Yet, the data fit in Zone A is approximately a factor two worse in comparison. This may be explained by poor discretization of the bathymetry using a finite-

Figure 13: *Measured and calculated inline electric field data for the ensemble of best fit resistivity models at all stations. Note, p01FR through p06FR were fit without a variation of x_a. For the remaining stations, the black lines represent the forward calculated data where $x_a = 3600$ m, red lines models where $x_a = 3700$ m. Error estimates are indicated by error bars.*

difference grid or the more complicated subsurface resistivity structure in the coastline vicinity that is not adequately represented by the simplified 2D resistivity models used in this study. The three remaining model parameters of the best fit models are interpreted as follows. In Zone A, the equivalent models indicate the freshwater aquifer at a depth of $d_1 \leq 80$ m, whereas Zone B allows the aquifer to be located at depths of up to $d_1 = 100$ m. For $x_a = 3700$ m, a value of $d_1 = 100$ m is even considered most likely, as all equivalent models (except one) map the aquifer at this depth. For $x_a = 3600$ m, d_1 may be found in the entire investigated model parameter space. The best fit model is found for $d_1 = 70$ m (black markers in Fig. 12c). This value corresponds to the results obtained in Zone A, which may indicate that the aquifer does not progress parallel to the sea surface, but rather, follows the bathymetry. Further consistencies between the stations of Zone A and Zone B are found in the resistivity and thickness of the freshwater aquifer (ρ_2 and d_2). The best fit model is found for an aquifer resistivity of $\rho_2 = 30$ Ωm and thickness of $d_2 = 100$ m. Both parameters are rather poorly determined for models with $x_a = 3600$ m due to the large variation across the entire investigated model parameter space. In contrast, the models where $x_a = 3700$ m exhibit a more restricted variation of ρ_2, but allow d_2 to also spread across the entire model parameter space.

Measured and calculated data from all receiver stations are displayed in Fig. 13. Note, synthetic

data in Zone A (p01FR through p06FR) are independent of x_a and are displayed in black. Calculated data of Zone B is represented for $x_a = 3600$ m in black and $x_a = 3700$ m in red. Although the subsurface resistivity structure is represented by very simplistic 2D models, the measured DED data is well represented. Exceptions are stations p02NR, p06FR, p16NR and p17NR, where the data is not fit within the error estimates at early times. In part, this also explains the inferior overall data fit obtained in Zone A (cf. Fig. 12) where 2 of 6 stations are only moderately represented by the forward models. A qualitative analysis of station p07FR through p17NR shows a superior data fit for models with $x_a = 3700$ m (red) compared to models with $x_a = 3600$ m (black). This is also supported by the χ value of the best fit models in Fig. 12.

The resistivity model that achieved the lowest overall χ is utilized to determine whether a brackish water zone exists at the head of the aquifer, representing a scenario where the groundwater aquifer is susceptible to seawater intrusion. The applied 2D resistivity model has fixed parameters $\rho_1 = 1.4$ Ωm, $\rho_2 = 30$ Ωm, $d_1 = 100$ m, $d_2 = 100$ m, and $x_a = 3700$ m. Also, resistivity of land and sea stay fixed to the values of the preceding study. The additional block is introduced to the model at the head of the western aquifer boundary. As illustrated in Fig. 14a, the block extends from 3700 m to a length defined by dx_b. The lateral extent of the block is varied between values of $dx_b = [100,\ 300,\ 500,\ 700,\ 900]$ m. The resistivity of the block is denoted the value ρ_b and varied between values of $\rho_b = [0.7,\ 1.4,\ 3.0,\ 5.0,\ 10.0]$ Ωm. For each possible combination of ρ_b and dx_b, data fits are calculated at each station of Zone B to investigate whether a data fit improvement is reached for specific combinations. For comparison, the value $\rho_b = 1.4$ Ωm simulates a closed aquifer scenario as it equals the value of the background sediments. In case $\rho_b = 0.7$ Ωm, the head of the aquifer is more conductive than the background, which is considered unrealistic, but was tested to cover a broader range of possibilities. In contrast, if $\rho_b = [3,\ 5,\ 10]$ Ωm, a brackish water body within the specified resistivity range of Kafri and Goldman (2006) exists at the aquifer head.

Figure 14: *(a) 2D resistivity model and (b-f) data misfit (χ) sorted from top to bottom by values of dx_b. The corresponding data misfit for different values of ρ_b are illustrated by solid black, dashed black and gray lines as labeled in the key. Station numbers 07 through 17 are illustrated in (b) through (f) at their corresponding position along the profile.*

The variations of dx_b will investigate the lateral extent of this zone towards the sea.

The corresponding data fits are displayed as a function of receiver position along the profile in Fig. 14b through f. The sub-figures are sorted for values of dx_b in ascending order. Each figure contains five lines representing the data misfit of one specific value of ρ_b. The gray lines show the data fit for values of $\rho_b = [0.7,\ 5,\ 10]$ Ωm, which are all inferior compared to the best fit 2D resistivity model without the additional block. The solid black line represents the data misfit for $\rho_b = 1.4$ Ωm, which corresponds to the previous modeling study. The dashed black line is the data misfit for $\rho_b = 3.0$ Ωm. In each figure, the numbers highlight the station location along the profile for easier interpretation. Note, x-scale of plots Fig. 14b through f are narrower than Fig. 14a.

Provided the lateral extent (dx_b) of the additional body is limited to less than 300 m, the data fit for all investigated models are practically identical at stations located more than 3900 m or more from the coastline. In case the body extends to greater lateral dimensions, all stations are influenced by its presence if $\rho_b > 1.4$ Ωm. The resulting χ curves show that a 2D block with a resistivity of $\rho_b = 10$ Ωm or $\rho_b = 0.7$ Ωm are the least likely scenarios for station p07FR through p15FR. In these scenarios, the data fit increases at every receiver station with the exception of p12NR located at 3650 m. At this station, a minimum χ is reached for $\rho_b = 10$ Ωm. In contrast, values of $\rho_b = 3$ Ωm

or $\rho_b = 5$ Ωm improve the overall data fit if the lateral extent of dx_b is confined to less than 100 m. Especially $\rho_b = 3$ Ωm tends to improve the overall data fit for stations located between 3400 m and 3900 m. However, the data fit is slightly inferior when $\rho_b = 1.4$ Ωm. An exception is Station 08 where the data fit remains superior compared to the open aquifer scenario. Between 3900 m and 4100 m, models with $\rho_b = 1.4$ Ωm achieve the best overall data fit. This indicates that if present, the lateral extent of the brackish water zone of 3 Ωm is likely confined to less than 300 m. Hence, a best fit 2D resistivity model is obtained for a block with lateral dimensions of $dx_b \leq 300$ m and a resistivity $\rho_b = 3$ Ωm. Consequently, the presented DED data set favors an open aquifer scenario which we interpreted as the most likely hydro-geological setting for the region of Bat Yam. Yet, this can only be seen as an indication favoring one possible hydro-geological scenario. On the basis of the presented forward modeling study, further groundwater flow modeling studies similar to Amir et al. (2013) are feasible to investigate the conditions at the western aquifer boundary. Final certainty regarding the true condition at the freshwater-seawater interface can ultimately only be achieved by in-situ measurements, such as borehole data. In this case, the DED measurements proved useful, as the aquifer boundary location is now determined between 3600 m and 3700 m.

The interpretation of measured DED data, both 1D and 2D, allowed us to delineate a resistive freshwater aquifer beneath the Mediterranean seafloor in the coastal vicinity of Bat Yam. The existence of this phenomenon has also been previously discovered by marine LOTEM measurements (Goldman et al., 2011; Lippert, 2015) and is now confirmed by the DED data. Its existence is therefore regarded as reliable. The 1D resistivity models indicate that this resistive body is detected at all stations located on the land-side of the No-Anchor-Zone (Zone A). However, due to the bathymetry in the direct coastal vicinity, reliable values for resistivity and thickness of individual layers in a 1D inversion model are difficult to derive (Haroon, 2016). Consequently, a 2.5D forward modeling approach using the 3D finite difference algorithm of Druskin and Knizhnerman (1988, 1994) was

Figure 15: *Final 2D resistivity model derived from the 2.5D forward modeling approach that best describes the measured DED data from Bat Yam, Israel. Note, displayed aquifer outlines are the maximum values of* d_1 *and* d_2 *and may actually be shallower and thinner.*

applied to consider the subsurface resistivity structure in a more realistic manner. Yet, without a finite-element algorithm it remains difficult to discretize the bathymetry accurately.

By applying a 2.5D forward modeling studies, a subsurface resistivity distribution was derived that adequately represents the measured DED data. The final 2D resistivity model is illustrated in Fig. 15. The 2.5D forward modeling approach was effective in delineating the lateral extent of the sub-seafloor aquifer system, but is cumbersome, ineffective, and not suitable as a standard interpretation scheme. The 425,600 forward calculations were conducted on the CHEOPS Cluster at the University of Cologne and took approximately three months. Future developments need to focus on developing 2D or even 3D inversion algorithms for DED in order to benefit from the increased lateral sensitivity of the method.

DISCUSSION

Previous marine LOTEM measurements were effective in detecting a sub-seafloor aquifer in the region of Bat Yam, Israel. The acquired LOTEM data lacked the necessary station density to determine the mechanism controlling its occurrence. Therefore, a novel EM method called DED was developed to fundamentally predict whether this sub-seafloor freshwater body is exposed to seawater intrusion. For this purpose, a new fixed-offset, seafloor-based DED transmitter/receiver system

was designed and built at the IGM Cologne. In this fixed-offset configuration, the inline electric field is sensitive towards 2D resistivity structures and profile curves are applicable to locate lateral resistivity discontinuities. This applies to both 2D and 3D structures that may represent groundwater bodies or hydrocarbon reservoirs (Haroon et al., 2016).

First marine DED measurements were carried out near the Mediterranean shoreline of Israel in April 2016. During the four-day campaign, 11 transmitter positions with 17 interpretable receiver stations were measured on the profile of Lippert (2015). The measured transients exhibit similar features as the synthetic data that were calculated using previously derived 2D resistivity models from LOTEM data (Lippert, 2015). Profile curves of the measured data show a clear indication of a lateral resistivity discontinuity between a conductive media interpreted as seawater saturated sediments in the West and a resistive body interpreted as the freshwater aquifer in the East.

The measured data were first interpreted using 1D inversion. The obtained inversion models show a resistive layer in the depth range of the expected freshwater body for stations located in Zone A, east of the No-Anchor-Zone. In turn, the stations located west of the No-Anchor-Zone did not require this resistive layer to achieve an adequate data fit which indicates a lateral resistivity contrast. The acquired model parameters from 1D inversion were utilized to determine 2D resistivity models for further investigations.

The response of 2D resistivity models were fit to measured data using the finite difference forward algorithm of Druskin and Knizhnerman (1988, 1994). In total, over 425,600 forward calculations were conducted for 11 transmitter positions. An ensemble of models was derived that adequately describe the measured DED data. The results for the receivers located in Zone B detect the aquifer boundary between 3600 m and 3700 m from the Israeli coast. Moreover, a preliminary interpretation of the hydro-geological setting at the western aquifer boundary was feasible. The

best data fit is achieved if the 2D resistivity model contains a further block of moderate resistivity ($\approx$ 3 Ωm) and a lateral extent of less than 300 m at the head of the aquifer. These resistivity values coincide with brackish water occurrences in the upper coastal sub-aquifers of Israel presented by Kafri and Goldman (2006). However, this hypothesis should be treated cautiously as a closed aquifer scenario achieves only slightly inferior data fit. In-situ measurements are necessary to further investigate this hypothesis. In this sense, the DED application was still justified as the lateral extent of the aquifer boundary is now confined between 3600 m and 3700 m from the coastline.

CONCLUSION

Overall, the novel DED system was successfully developed and applied for the first time in a shallow water environment. The acquired data enabled to detect and confine the lateral extent of the freshwater body underneath the Mediterranean Sea. The enhanced lateral sensitivity towards shallow resistive bodies justifies future applications in geophysical groundwater investigations near coastlines in the Middle East and in other regions across the globe. However, due to the inferior SNR compared to conventional methods utilizing a HED source, it remains questionable if DED is also applicable to effectively investigate deeper targets.

Future DED applications will need to address issues associated with the complicated measurement procedure, limited SNR, and rudimentary 1D interpretation scheme. Aside from the proposed hardware updates mentioned above, theoretical developments should be the main focus. The most obvious being the necessity of a 2D or 3D inversion software to account for the enhanced lateral sensitivity. The method is designed to detect lateral resistivity discontinuities more precisely, but the data interpretation is presently based on 1D inversion with subsequent 2.5D forward modeling. This approach is cumbersome, time-consuming and computationally expensive. A more sophisti-

cated 2D/3D inversion approach is needed to improve the interpretation of the acquired data.

ACKNOWLEDGEMENTS

This research was funded by the German Research Foundation (DFG) in the framework of the project TE170/19-1. We would like to thank one anonymous reviewer, Kurt Strack and Kerry Key for their comments in the review process. Their suggestions helped to substantially improve the original manuscript. The authors would like to thank Katrin Schwalenberg (BGR), Sebastian Hölz (GEOMAR) and Tilman Hanstein (KMS Technologies) for their contribution in developing the DED system. We thank Itay Katzman and his crew at EcoOcean and Gideon Tibor from the IOLR for their assistance during the measurements. We thank Janine Böckmann, David Ossen, Nadine Pützer and Jan Wittke for their devoted effort during the measurements.

REFERENCES

Amir, N., U. Kafri, B. Herut, and E. Shalev, 2013, Numerical Simulations of Submarine Groundwater Flow in the Coastal Aquifer at the Palmahim Area, the Mediterranean Coast of Israel: Water Resources Management, **27**, 4005–4020.

Archie, G. E., 1942, The Electrical Resistivity Log as an Aid in Determining Some Reservoir Characteristics: Trans. Am. Inst. Min. Metal. and Petr. Eng., **146**.

Bhuiyan, A., E. Vesteras, and A. McKay, 2014, Towed Streamer EM data from the Barents Sea, Norway: Presented at the SEG Denver Annual Meeting.

Bubnov, V. P., V. Goldansky, A. S. Kashik, M. M. Mandelbaum, N. Rykhlinski, and V. V. Chemyak, 1984, Spatial differentiation in electric survey [in Russian]: Russian Geology and Geophysics, **6**, 106–111.

Chave, A. D., and C. S. Cox, 1982, Controlled Electromagnetic Sources for Measuring Electrical Conductivity Beneath the Oceans: 1. Forward Problem and Model Study: Journal of Geophysical Research, **87**, 5327–5338.

Chen, J., and D. L. Alumbaugh, 2011, Three methods for mitigating airwaves in shallow water marine controlled-source electromagnetic data: Geophysics, **76**, F89–F99.

Constable, S., 2010, Ten years of marine CSEM for hydrocarbon exploration: Geophysics, **75**, A67–A81.

Constable, S. C., R. L. Parker, and C. G. Constable, 1987, Occam's Inversion: A practical algorithm for generating smooth models from electromagnetic sounding data: Geophysics, **52**, 289–300.

Davydycheva, S., A. Kaminsky, N. Rykhlinski, and A. Yakovlev, 2015, A large-scale field study in eastern siberia using novel time-domain electromagnetic technology: Interpretation, **3**, T109 – T120.

Davydycheva, S., and N. Rykhlinski, 2009, Focused Source EM Survey - New Solution for Both

Shallow and Deep Water: Presented at the 71st EAGE Conference and Exhibition incorporating SPE EUROPEC 2009.

———, 2011, Focused-source electromagnetic survey versus standard CSEM: 3D modeling in complex geometries: Geophysics, **76**, F27–F41.

Davydycheva, S., N. Rykhlinski, and P. Y. Legeydo, 2006, Electrical-prospecting method for hydrocarbon search using the induced-polarization effect: Geophysics, **71**, G179–G189.

Druskin, V. L., and L. A. Knizhnerman, 1988, Spectral differential-difference method for the numeric solution of three-dimensional nonstationary problems of electric prospecting: Izvestiya: Earth Physics, **24**, 641–648.

———, 1994, Spectral approach to solving three-dimensional Maxwell's diffusion equations in the time and frequency domains: Radio Science, **29**, 937–953.

Edwards, R. N., 1997, On the resource evaluation of marine gas hydrate deposits using seafloor transient electric dipole-dipole methods: Geophysics, **62**, 63–74.

Eidesmo, T., S. Ellingsrud, L. M. MacGregor, S. Constable, S. A. Sinha, S. Johansen, F. N. Kong, and H. Westerdahl, 2002, Sea Bed Logging (SBL), a new method for remote and direct identification of hydrocarbon filled layers in deepwater areas: First Break, **20**, 144–152.

Ellingsrud, S., T. Eidesmo, S. Johansen, M. C. Sinah, L. M. MacGregor, and S. Constable, 2002, Remote sensing of hydrocarbon layers by seabed logging (SBL): Results from a cruise offshore Angola: The Leading Edge, **21**, 972–982.

Goldman, M., A. Arad, U. Kafri, D. Gilad, and A. Melloul, 1988, Detection of fresh-water/seawater interface by the time domain electromagnetic (TDEM) method in Israel: Presented at the Proc. 10th SWIM, Ghent.

Goldman, M., E. Levi, B. Tezkan, and P. Yogeshwar, 2011, The 2D coastal effect on marine time domain electromagnetic measurements using broadside dBz/dt of an electrical transmitter dipole:

Geophysics, **76**, F101–F109.

Haroon, A., 2016, Development of Novel Time-Domain Electromagnetic Methods for Offshore Groundwater Studies: A Data Application from Bat Yam, Israel: PhD thesis, University of Cologne.

Haroon, A., V. Mogilatov, M. Goldman, R. Bergers, and B. Tezkan, 2016, Exploration of resistive targets within shallow marine environments using the Circular Electrical Dipole and the Differential Electrical Dipole methods: A time-domain modelling study: Geophysical J. Int., **205**, 1032–1048.

Hölz, S., A. Swidinsky, M. Sommer, M. Jegen, and J. Bialas, 2015, The use of rotational invariants for the interpretation of marine CSEM data with a case study from the North Alex mud volcano, West Nile Delta: Geophysical J. Int., **201**, 224–245.

Hördt, A., V. L. Druskin, L. A. Knizhnerman, and K. M. Strack, 1992a, Interpretation of 3-D effects in long-offset transient electromagnetic (LOTEM) soundings in the Muensterland area/Germany: Geophysics, **57**, 1127–1137.

Hördt, A., H. Joedicke, K. M. Strack, K. Vozoff, and P. A. Wolfgram, 1992b, Inversion of long-offset tem soundings near the borehole muensterland 1, germany, and comparison with mt measurements: Geophysical Journal International, **108**, 930–940.

Jupp, D. L. B., and K. Vozoff, 1975, Stable Iterative Methods for the Inversion of Geophysical Data: Geophys. J. R., **42**, 957–976.

Kafri, U., and M. Goldman, 2006, Are the lower subaquifers of the Mediterranean coastal aquifer of Israel blocked to seawater intrusion? Results of TDEM (time domain electromagnetic study): Israel Journal of Earth and Science, **55**, 55–68.

Kapuler, Y., and J. Bear, 1970, Numerical solutions to the movement of the interface in a multi-layered coastal aquifer: Tahal, Water Planning for Israel. Rep. 01/74/70 (in Hebrew).

Key, K., 2016, MARE2DEM: a 2-D inversion code for controlled-source electromagnetic and magnetotelluric data: Geophysical Journal International, **207**, 571–588.

Kolton, Y., 1988, Examination of the connection between seawater in the Pleistocene aquifer in the Mediterranean shelf of central Israel.: Tahal, Water Planning for Israel. Rep. 01/88/31 (in Hebrew).

Legeydo, P. Y., M. M. Mandelbaum, and N. Rykhlinski, 1990, Application of differentially adjusted electric exploration of the Nepa Dome [in Russian]: Soviet Geology and Geophysics, **31**.

———, 1997, Results of a differential-normalized electrical prospecting in the Central part of the Nepa arch on the Siberian platform [in Russian]: Russian Geology and Geophysics, **38**, 1707–1713.

Lippert, K., 2015, Detektion eines submarinen Aquifers vor der Küste Israels mittels mariner Long Offset Transient-elektromagnetischer Messung: PhD thesis, University of Cologne.

Lippert, K., B. Tezkan, R. Bergers, and M. Goldman, 2012, Erkundung eines Aquifers unter dem Mittelmeer vor der israelischen Küste mit Long Offset Transient Elektromagnetik: Presented at the 72. Jahrestagung der Deutschen Geophysikalischen Gesellschaft.

Mandelbaum, M. M., E. B. Ageenkov, P. Y. Legeydo, P. Y. Perserev, and N. Rykhlinski, 2002, Normalized-differential electrical measurements in hydrocarbon exploration: the state of the art and prospects for future: Russian Geology and Geophysics, **43**, 1085–1143.

Mogilatov, V., 1992, A circular electrical dipole as a new source in electric surveys.: Izvestiya: Physics of the solid Earth, **6**, 97–105.

Mogilatov, V., and B. Balashov, 1996, A new method of geoelectrical prospecting by vertical electric current soundings: Journal of Applied Geophysics, **36**, 31–41.

Mogilatov, V., M. Goldman, M. Persova, Y. Soloveichik, Y. Koshkina, O. Trubacheva, and A. Zlobinskiy, 2016, Application of the marine circular electric dipole method in high latitude arctic

regions using drifting ice floes: Journal of Applied Geophysics, **135**, 17 – 31.

Munkholm, M., and E. Auken, 1996, Electromagnetic Noise Contamination on Transient Electromagnetic Soundings in Culturally Distrubed Environments: Journal of Environmental Engineering Geophysics, **1**, 119–127.

Rykhlinskaya, E., and S. Davydycheva, 2014, Method for marine geoelectrical exploration with electrical current focusing. (US Patent 8, 762,062).

Scholl, C., 2005, The influence of multidimensional structures on the interpretation of LOTEM data with one-dimensional models and the application to data from Israel: PhD thesis, University of Cologne.

Scholl, C., and R. N. Edwards, 2007, Marine downhole to seafloor dipole-dipole electromagnetic methods and the resolution of resistive targets: Geophysics, **72**, WA39–WA49.

Schwalenberg, K., and M. Engels, 2011, Marine Controlled Source Electromagnetic Methods for Gas Hydrate Assessment: New Instrumentation and First Results from the Black Sea Test Cruise: Presented at the 24. Kolloquium Elektromagnetischer Tiefenforschung, Neustadt.

Sherman, D., P. Kannberg, and S. Constable, 2017, Surface towed electromagnetic system for mapping of subsea arctic permaforst: Earth and Planetary Science Letters, **460**, 97–104.

Strack, K. M., 1992, Exploration with deep transient electromagnetics: Elsevier.

Strack, K. M., N. Allegar, and S. Ellingsrud, 2008, Marine time domain csem: an emerging technology: SEG Annual Meeting, Las Vegas, 653–656.

Swidinsky, A., S. Hölz, and M. Jegen, 2012, On mapping seafloor mineral deposits with central loop transient electromagnetics: Geophysics, **77**, E171–E184.

Tezkan, B., K. Lippert, R. Bergers, and M. Goldman, 2012, On the exploration of a marine aquifer offshor Israel by long offset transient electromagnetic: A 2D conductivity model: Presented at the 21st EM Induction Workshop,.

Thomsen, L., D. Meaux, C. Weiss, A. Sharma, N. Allegar, and K. M. Strack, 2007, Novel marine electromagnetics: from deep into shallow water: Presented at the SEG Annual Meeting, San Antonio.

Veeken, P. C. H., P. Y. Legeydo, Y. A. Davidenko, E. O. Kudryavceva, S. A. Ivanovm, and A. Chuvaev, 2009, Benefits of the induced polarization geoelectric method to hydrocarbon exploration: Geophysics, **74**, B47–B59.

Weidelt, P., 2007, Guided Waves in marine CSEM: Geophysical J. Int., **171**, 153–176.

Weiss, C. J., 2007, The fallacy of the "shallow-water problem" in marine CSEM exploration: Geophysics, **72**, A93–A97.

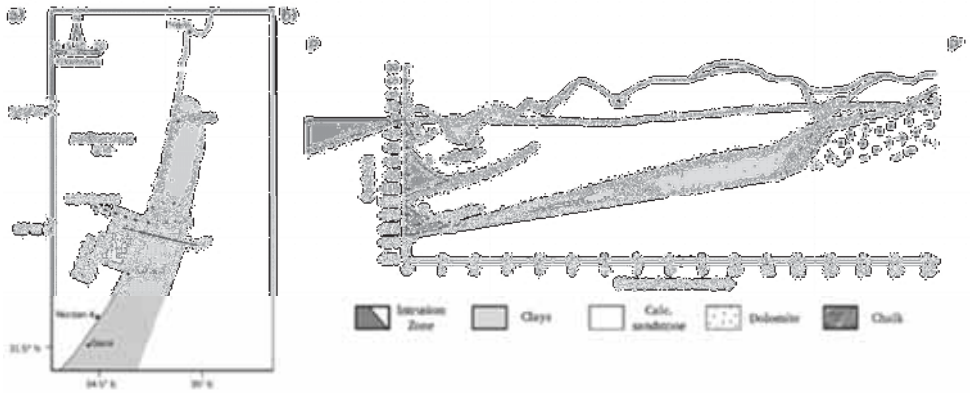

1 (a) Map of the coastal aquifer of Israel highlighted in dark-gray. The Palmahim area where the lower sub-aquifers are occupied by fresh water is illustrated in light-gray along with the measured DED profile (dashed black line). Image was modified after \cite{Amir:2013}. (b) Typical cross section of the Israeli coastal aquifer between P and P' indicated by the solid black line in (a). Near the coast, the aquifer is divided into four separate sub-aquifers named A through D that are divided by impermeable clay formations. Image modified after \cite{KafriGoldman:2006}.

45x18mm (300 x 300 DPI)

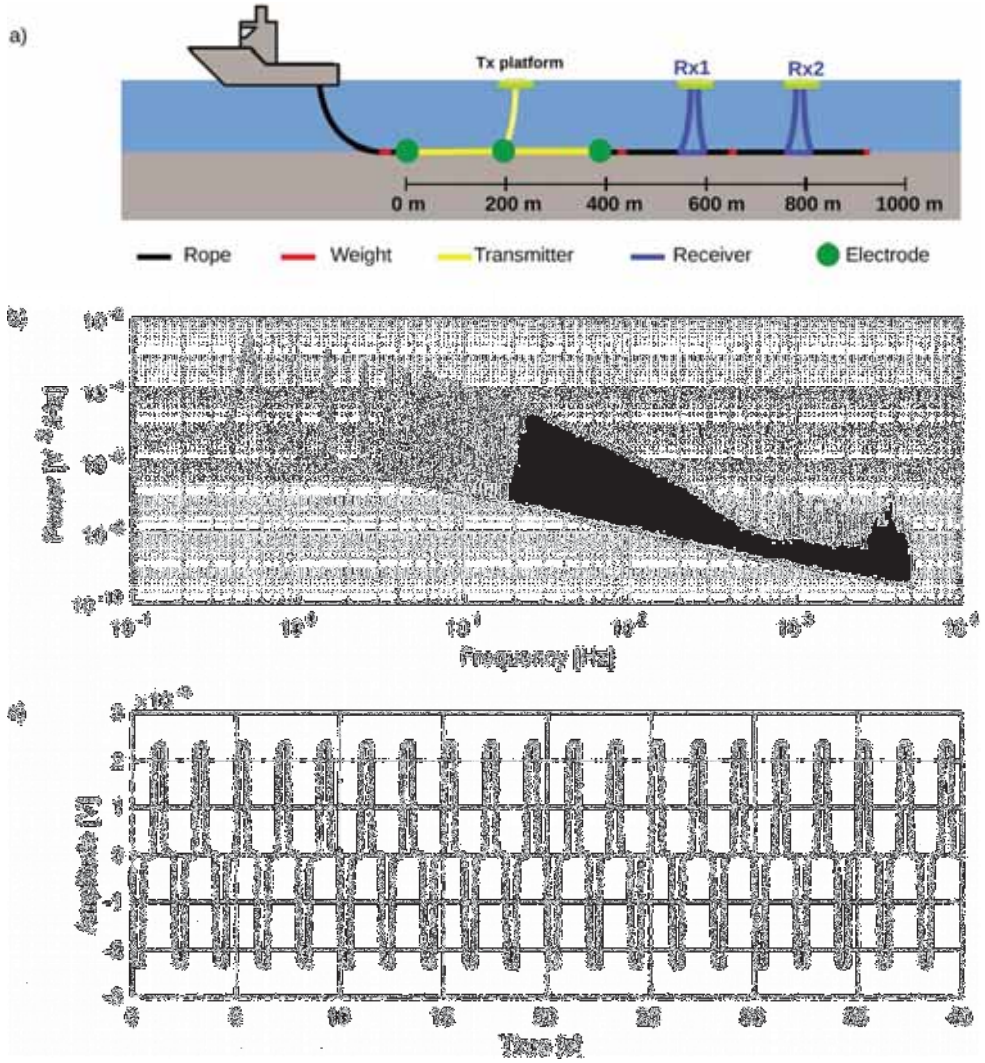

2 (a) Sketch of a seafloor-based DED transmitter/receiver system consisting of a 400 m double-dipole antenna (yellow) and two inline electric field receivers of 50 m length (blue) that are connected to the transmitter antenna by segments of rope/chain at offsets of 370 m and 580 m, respectively. Note, receiver electrodes are located on the seafloor. The signal is guided to the KMS-820 acquisition unit located on the sea-surface. (b) Power spectrum and (c) excerpt of a measured inline voltage time series for an exemplary station from Bat Yam, Israel. A 50% duty cycle current step-function with a period of 2 s was applied.

119x129mm (300 x 300 DPI)

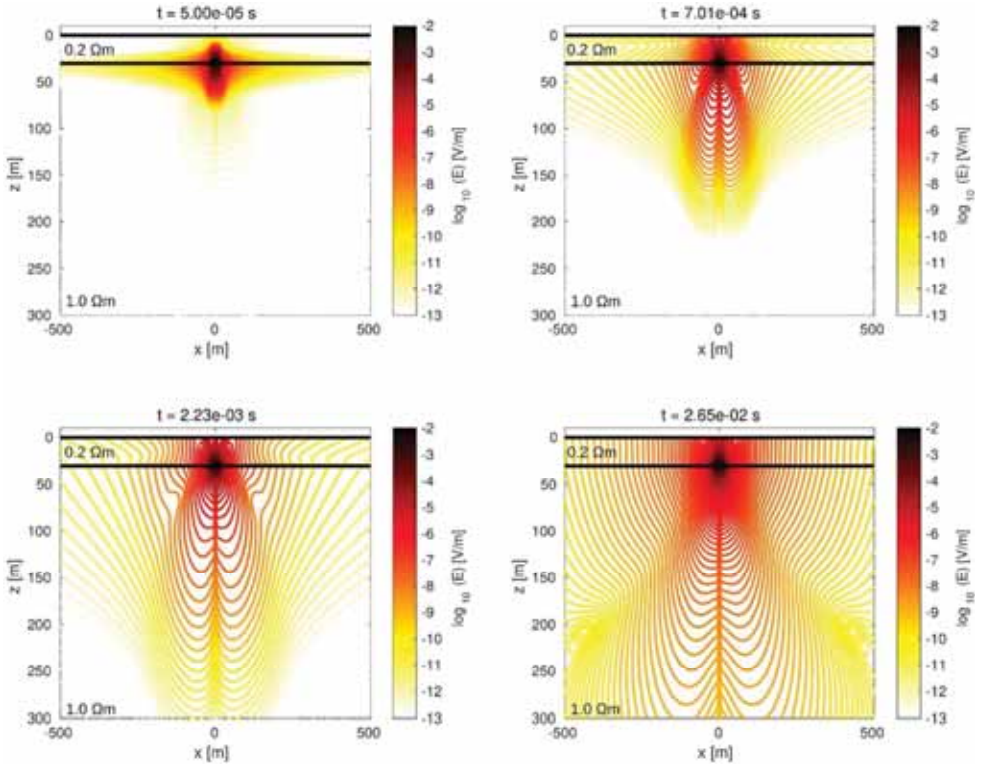

3 Electric field amplitude in the xz-plane for a source-normalized seafloor-based DED transmitter at time delays of t=5.00e^{-5} s, t=7.01e^{-4} s, t=2.23e^{-3} s and t=2.65e^{-2} s after the current is switched on. The resistivity of the overlying 30 m water column is 0.2 Ωm and underlying half-space is 1 Ωm. The insulating air (z < 0 m) is defined at 10^{8} Ωm. The black lines represent the horizontal layer boundaries of the sea surface (z = 0 m) and seafloor z = 30 m).

86x67mm (300 x 300 DPI)

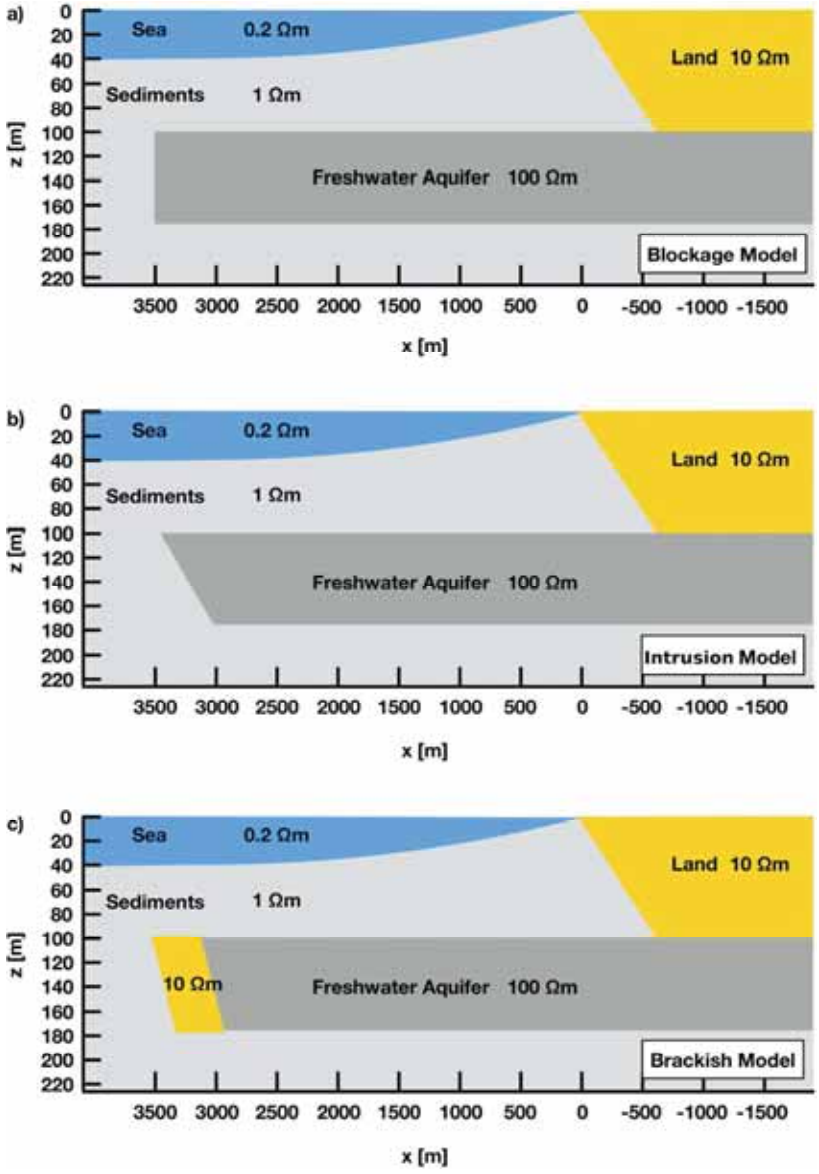

4 Schematics of possible 2D resistivity models found in the coastal vicinity of Bat Yam, Israel. (a) The aquifer is assumed to be blocked from seawater encroachment. (b) Typical wedge-shape boundary characterizes the transition between freshwater aquifer and seawater saturated sediments. (c) Brackish-water zone is located at the head of the freshwater body, representing an open aquifer scenario. Transmitter stations were simulated every 100 m between 2500 m and 4500 m with an electric field receiver located at an offset of 580 m on either side of the transmitter. Note, a more detailed illustration of the Tx/Rx configuration is found in Fig. 5.

122x175mm (300 x 300 DPI)

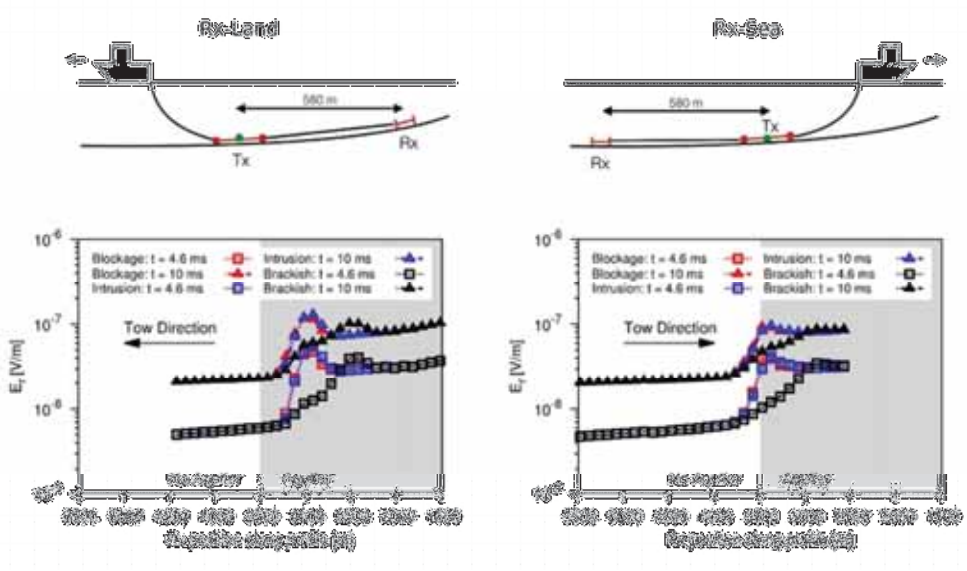

5 Profile plots at selected time-delays of 4.6~ms (squares) and 10~ms (triangles) after current is switched on. The Blockage, Intrusion, and Brackish-Water models of Fig. 4a, b, and c are displayed by red, blue, and black colors, respectively. In the left image the receiver is located between transmitter and shoreline (Rx-Land). In the right image the receiver is located towards the sea-side of the transmitter (Rx-Sea). The gray background color indicates the lateral extent of the freshwater aquifer.

64x38mm (300 x 300 DPI)

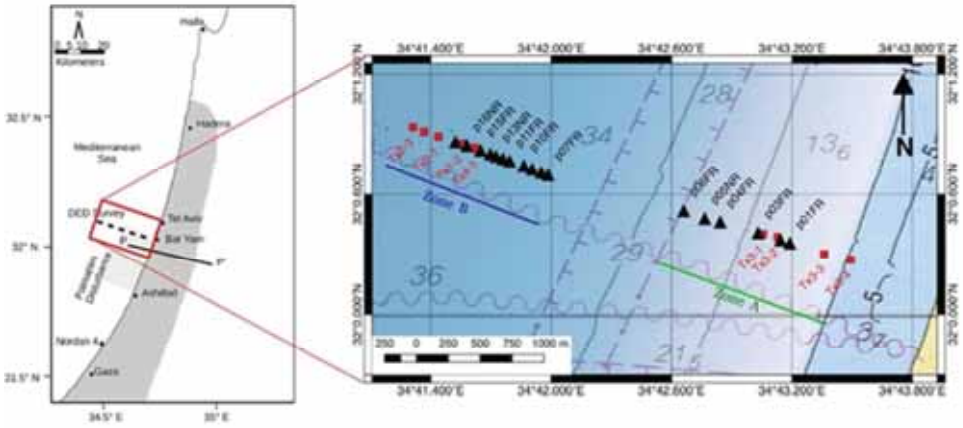

6 Map of the measurement area and survey geometry including positions of the measured inline receiver dipoles marked by black triangles and labeled p01FR through p17NR (from East to West). Transmitter centers are marked by red squares. The profile is interrupted due to a gas pipeline and a corresponding No-Anchor-Zone, which is bounded by the $\perp$ in the nautical map. Background map provided by the IOLR in Haifa. The left map of the coastal aquifer of Israel is modified after \cite{Amir:2013}.

50x23mm (300 x 300 DPI)

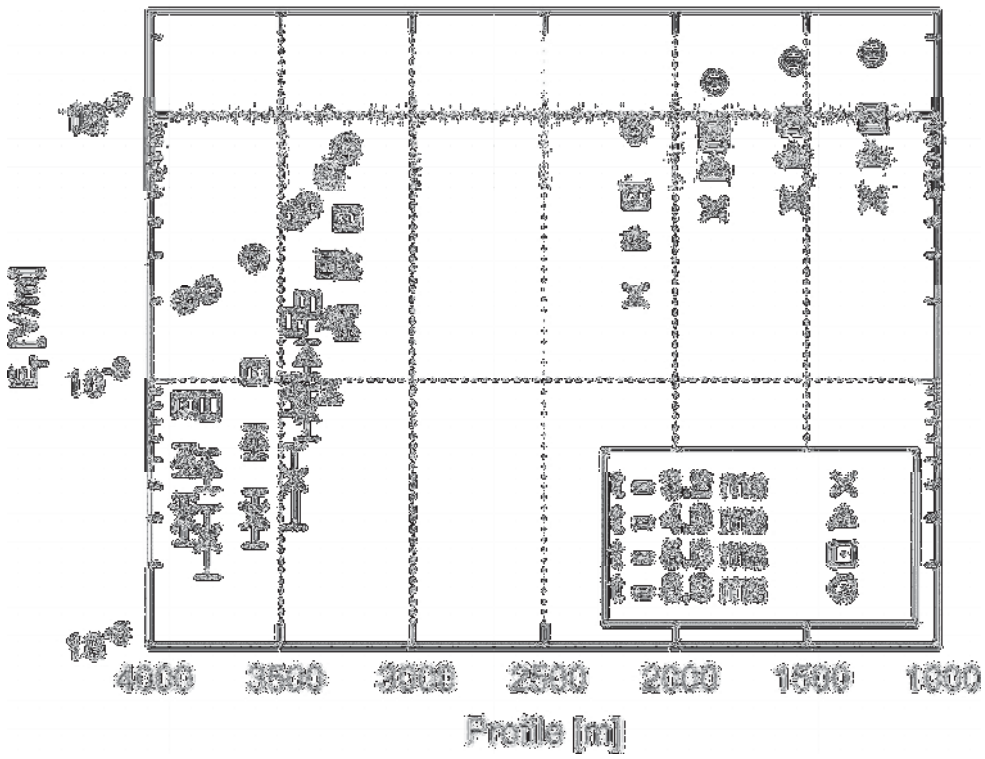

7 Profile plots at several time-delays derived from processed transients measured by the far receiver (FR) at an offset of 580 m. Data errors are indicated by the plotted error bars and are derived from the distribution of the measured signals in the robust stacking scheme (see text for further details).

65x50mm (300 x 300 DPI)

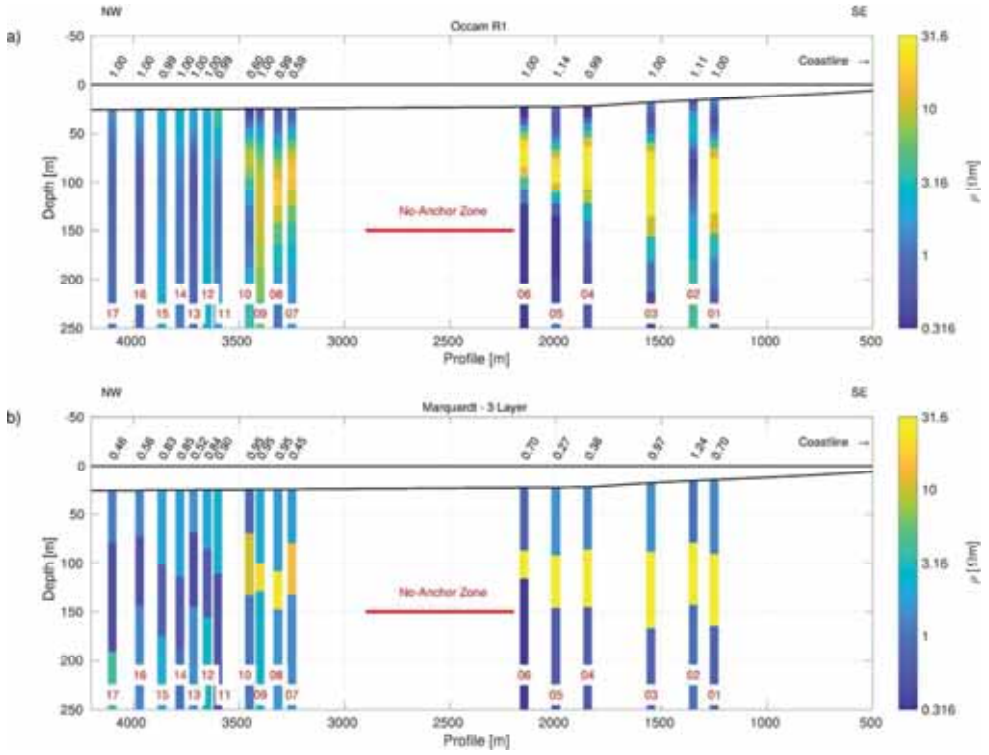

8 (a) 1D Occam and (b) Marquardt inversion models. The colored bars are located at the position of each corresponding receiver along the profile and describe the sub-seafloor resistivity structure. Light colors represent resistive, dark colors conductive structures. The data misfit is labeled above each graph. Stations are indicated by the red numbers at the bottom of each bar-graph.

84x64mm (300 x 300 DPI)

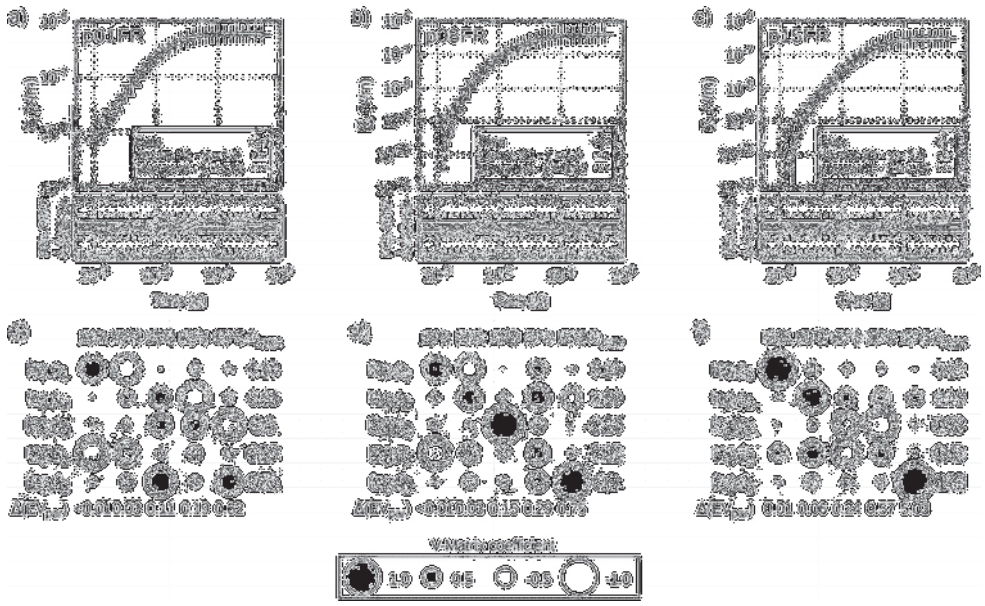

9 (a-c) Data misfit and (d-f) **V**-matrix coefficients for station p01FR (left), p08FR (center) and p15FR (right). The measured data in the top panel is displayed by black markers including the corresponding error estimates that are illustrated as error bars. The synthetic response is displayed by solid and dashed black lines for Occam and Marquardt models, respectively. Beneath each image in the top-panel, residual errors are plotted for better reference of the data fit. The shaded zone indicates where the measured data is fit within the error bounds at each datum. The bottom panel displays the coefficients of the **V**-matrix. Black circles represent positive, white circle negative values. The radius of each circle is proportional to the coefficient weight. For further details refer to text.

67x41mm (300 x 300 DPI)

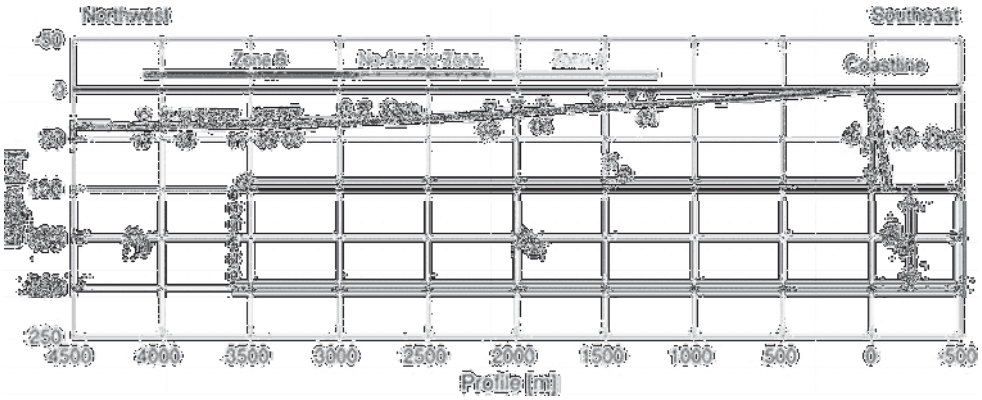

10 Sketch of the 2D resistivity model utilized in the 2.5D forward modeling study. The model parameters ρ_1, ρ_2, d_1, d_2, and x_a are varied while seawater and land resistivity remain constant at 0.2 Ωm and 10 Ωm, respectively. At the air interface, integral boundary conditions are applied. The black triangles indicated the receiver locations along the profile. Selected station numbers are displayed beneath for reference.

44x17mm (300 x 300 DPI)

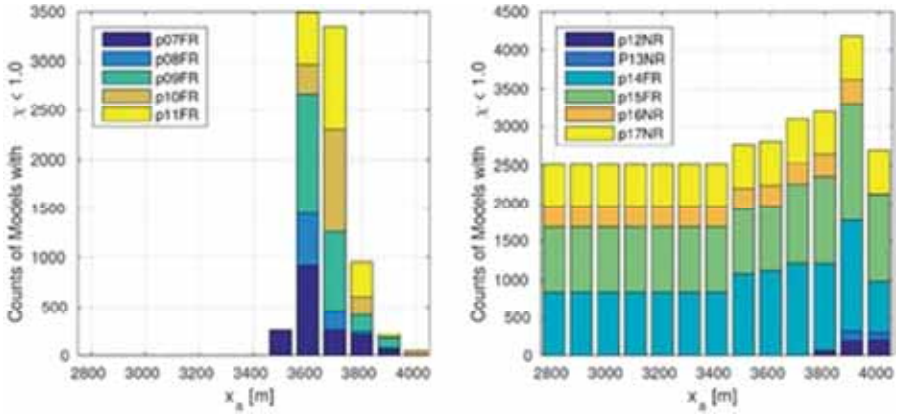

11 Bar graphs displaying the accumulation of models reaching $\chi \leq 1$ to identify the most likely position of the western aquifer boundary. The left figure shows stations p07FR through p11FR. The right image contains p12NR through p17NR. Each receiver is represented by a different color. In total, 58,240 forward models were tested at each receiver site.

38x17mm (300 x 300 DPI)

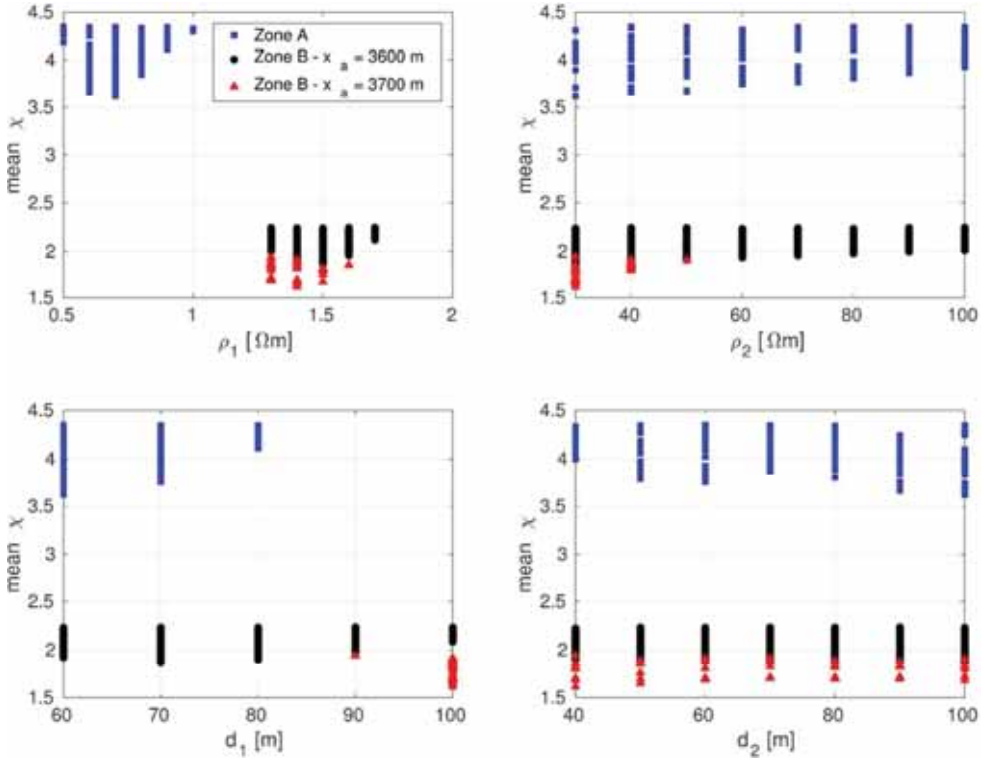

12 Scatter plots displaying model parameter distribution for the ensemble of best fit models: (a) ρ_1, (b) ρ_2, (c) d_1 and (d) d_2 vs. the data fit χ. The x-axis of each sub-figure displays the entire investigated model parameter space. The black and red markers represent the model parameter distribution for models with x_a=3600 m and x_a=3700 m, respectively. The blue markers show the model parameter distribution obtained for receivers located in Zone A.

85x66mm (300 x 300 DPI)

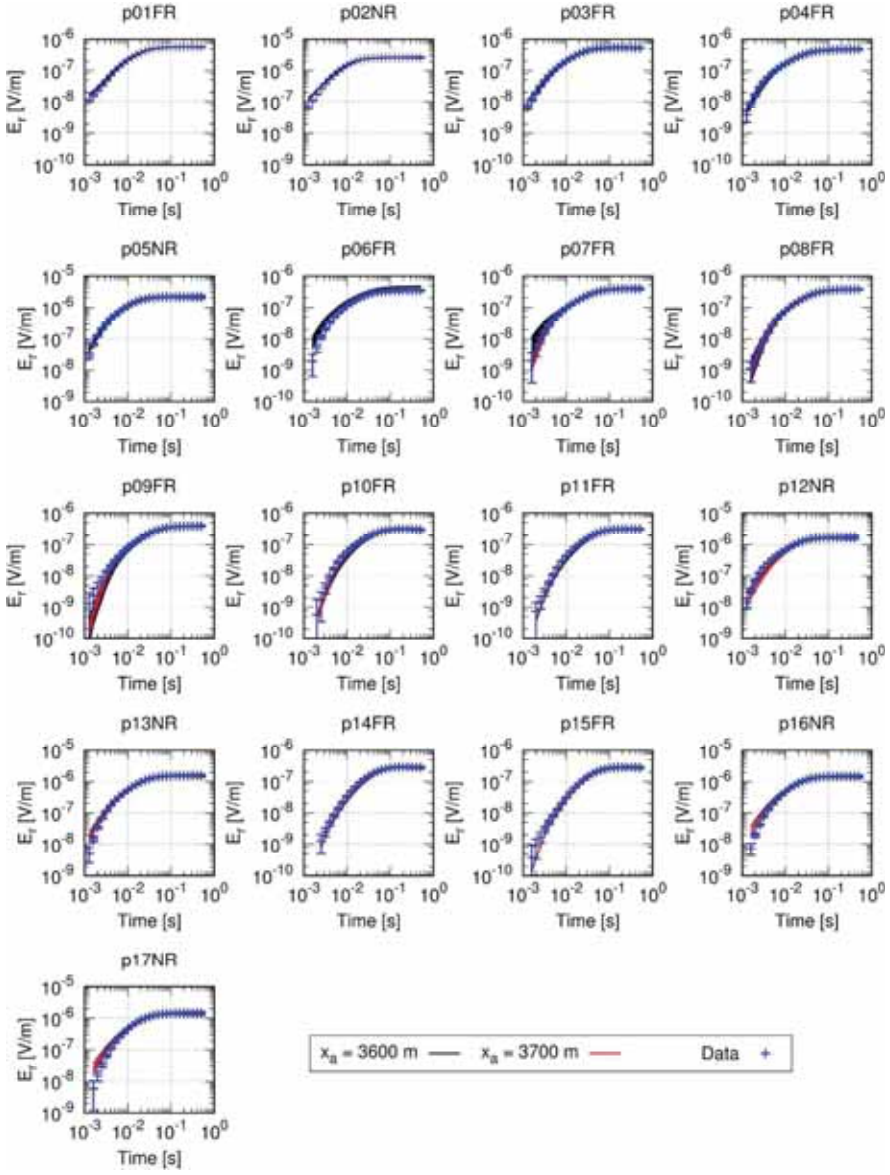

13 Measured and calculated inline electric field data for the ensemble of best fit resistivity models at all stations. Note, p01FR through p06FR were fit without a variation of x_a. For the remaining stations, the black lines represent the forward calculated data where x_a=3600 m, red lines models where x_a=3700 m. Error estimates are indicated by error bars.

146x194mm (300 x 300 DPI)

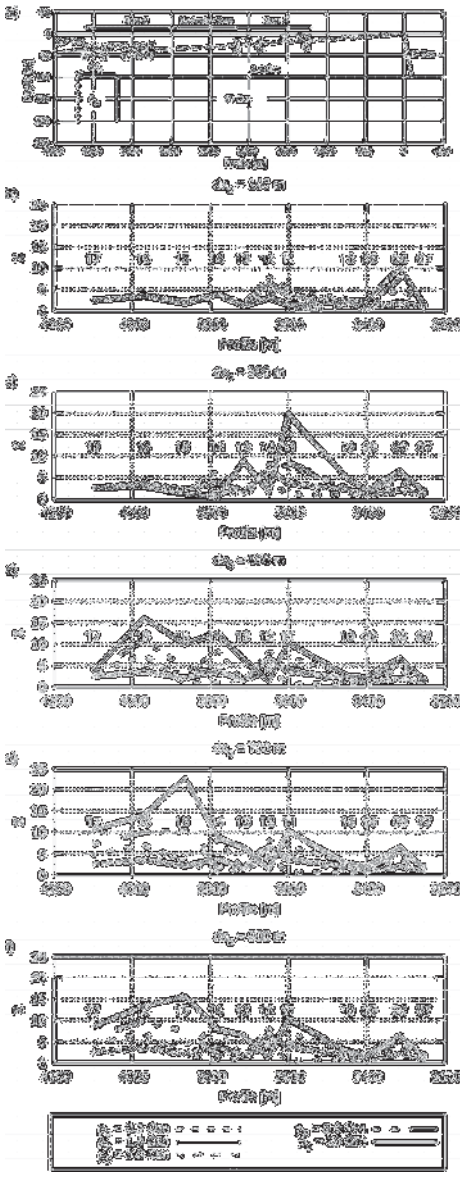

14 (a) 2D resistivity model and (b-f) data misfit χ sorted from top to bottom by values of dx_b. The corresponding data misfit for different values of ρ_b are illustrated by solid black, dashed black and gray lines as labeled in the key. Station numbers 07 through 17 are illustrated in (b) through (f) at their corresponding position along the profile.

282x725mm (300 x 300 DPI)

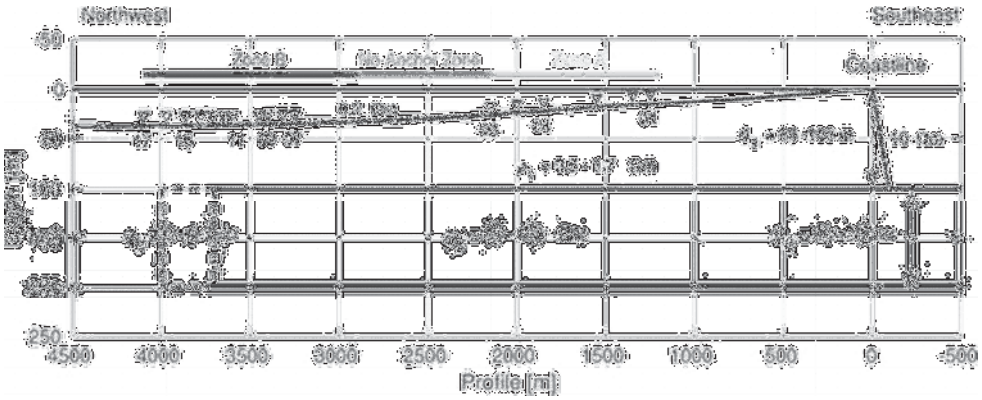

15 Final 2D resistivity model derived from the 2.5D forward modeling approach that best describes the measured DED data from Bat Yam, Israel. Note, displayed aquifer outlines are the maximum values of d_1 and d_2 and may actually be shallower and thinner.

44x17mm (300 x 300 DPI)